Supporting Information

Tuning the interfacial chemistry for stable and high energy density aqueous sodium-ion/sulfur batteries

UV-Vis and FT-IR study:

UV-Vis measurements were performed using Shimadzu UV-2600 spectrophotometer. FT-IR spectra (neat) were recorded using BRUKER TENSOR-II spectrometer in the range of 600−4000 cm^{-1} with a spectral resolution of 4 cm^{-1} and 100 scans. The obtained data were collected and analyzed by OPUS software. The Na-ion conductivity of electrolyte was tested by Metrohm 912 conductivity meter

NMR analysis: ^{1}H and ^{23}Na NMR spectra were recorded using a JEOL JNM-ECS 400 spectrometer at ambient probe temperatures.

Thermogravimetric analysis (TGA):

The thermogravimetric analysis (TGA) was performed in the N_2 atmosphere using alumina pan using "TGA/DSC1" instrument from Mettler Toledo with SDTA sensor, and data were analyzed in STAR^{e} software (version 12.1). Thermal stability was investigated by heating from 30 °C to 800 °C at a heating rate of 10 °C/min at 40 mL/min N_2 (99.999%) flow. Each sample was tested for at least three times, and the error limit is <2%.

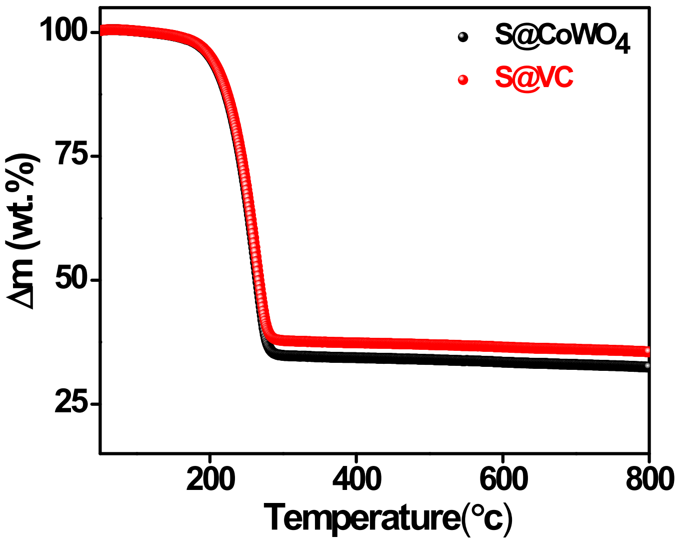

Fig. S1A. (a) TGA of $S@CoWO_4$ and S@VC.

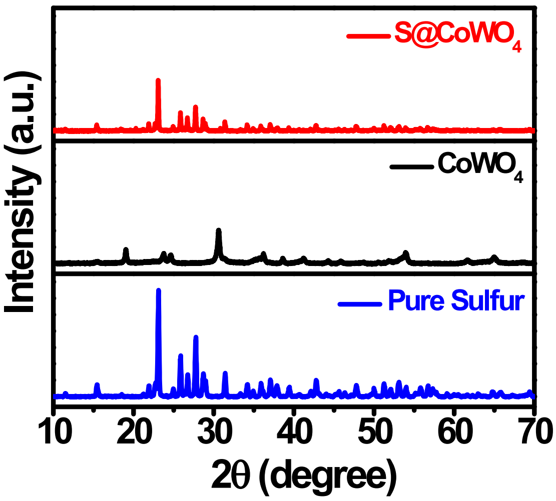

Fig. S1B. (a) XRD pattern of various catalysts.

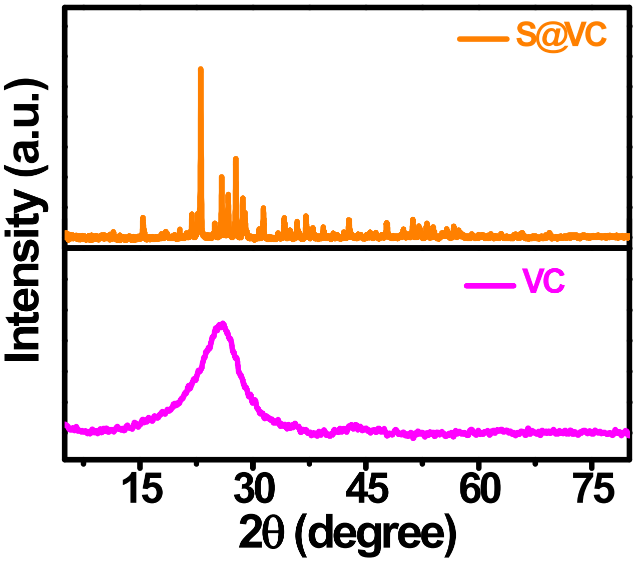

Fig. S1C. (a) XRD pattern of VC and S@VC.

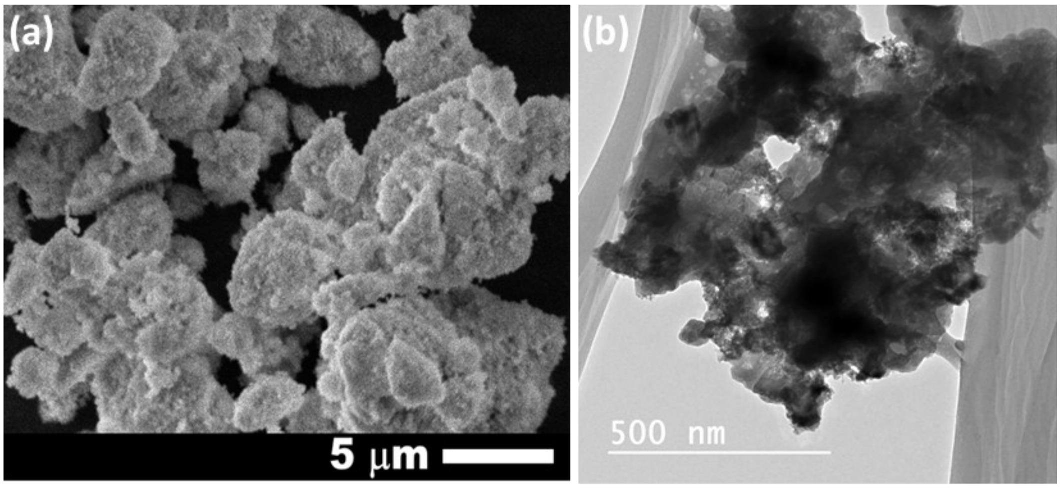

Fig. S2A. (a) SEM and (b) TEM images of S@$CoWO_4$.

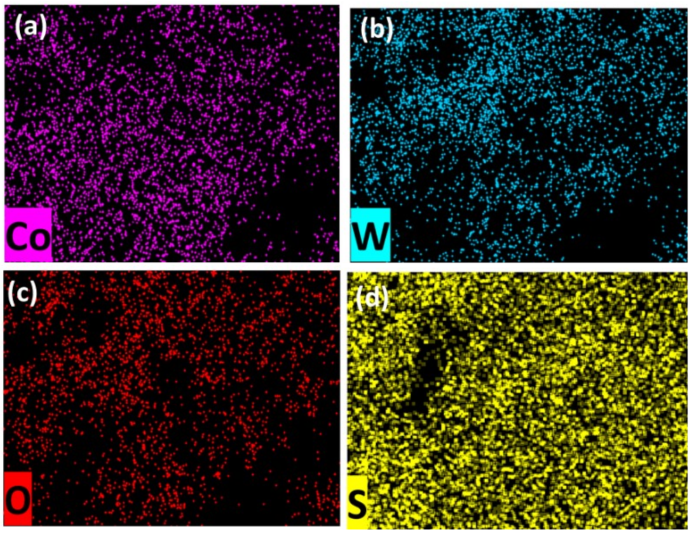

Fig. S2B. Elemental dot mapping images representing the distribution of (a) cobalt, (b) tungsten, (c) oxygen, and (d) sulfur, in S@$CoWO_4$.

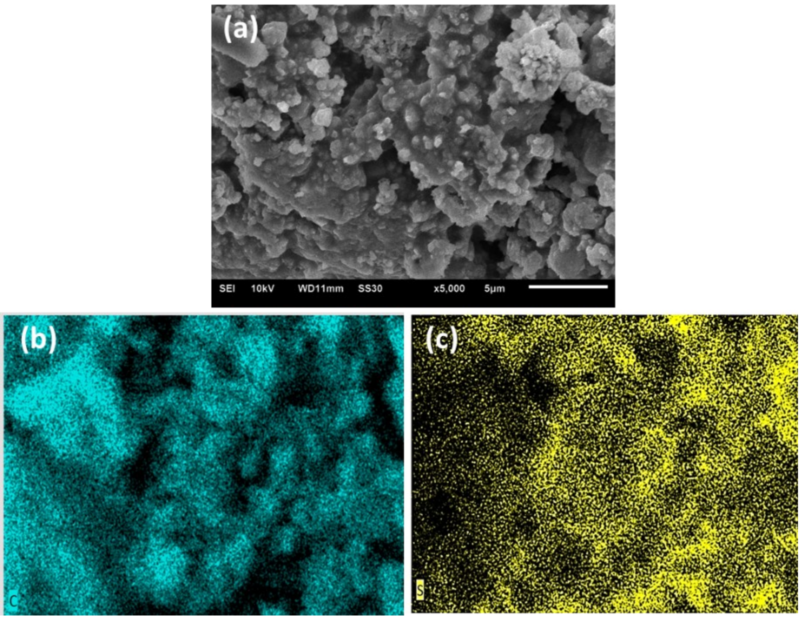

Fig. S2C. (a) SEM image, elemental dot mapping images showing the distribution of (b) carbon, and (c) sulfur in S@VC anode

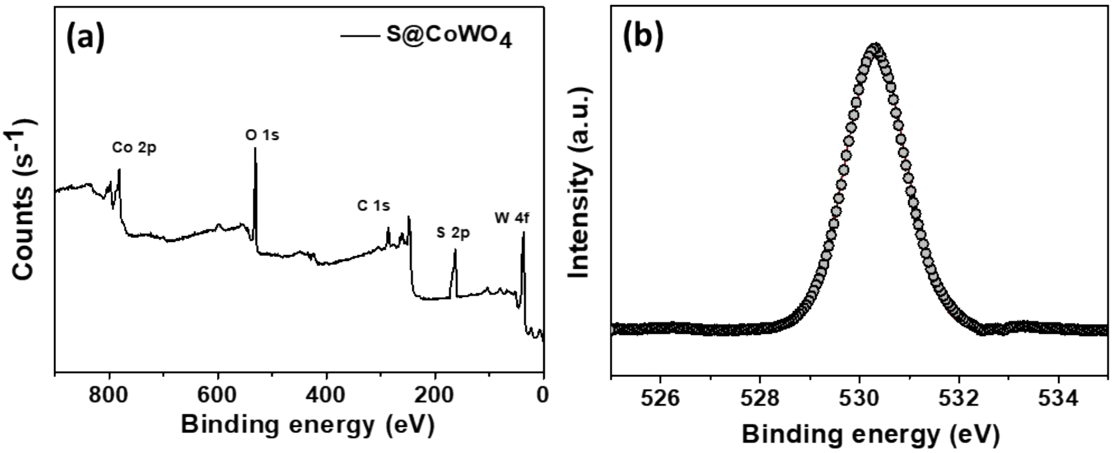

Fig. S3. (a) XPS survey spectra and deconvoluted XPS spectra of (b) O 1s for S@$CoWO_4$.

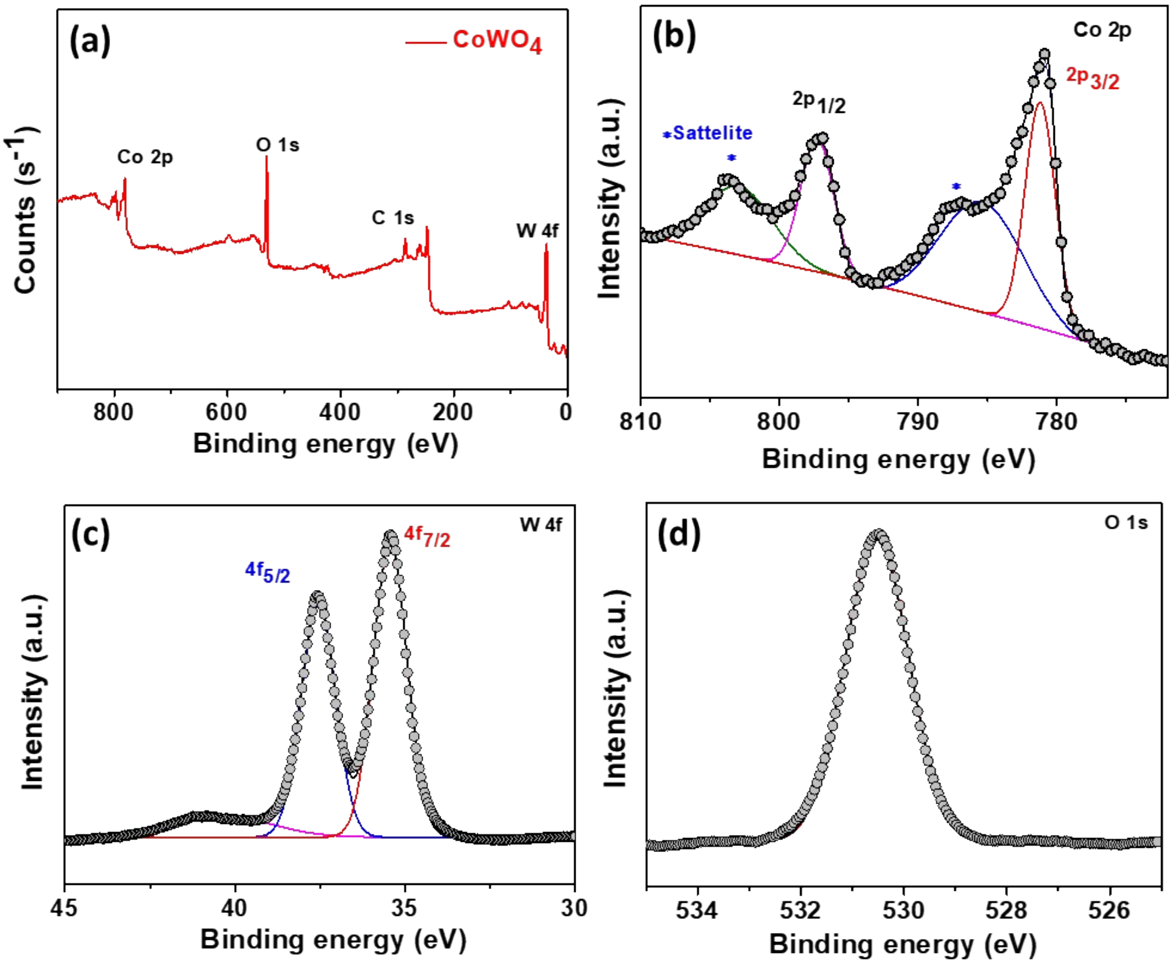

Fig. S4. (a) XPS survey spectrum and deconvoluted XPS spectra of (b) Co 2p, (c) W 4f and (d) O 1s of $CoWO_4$.

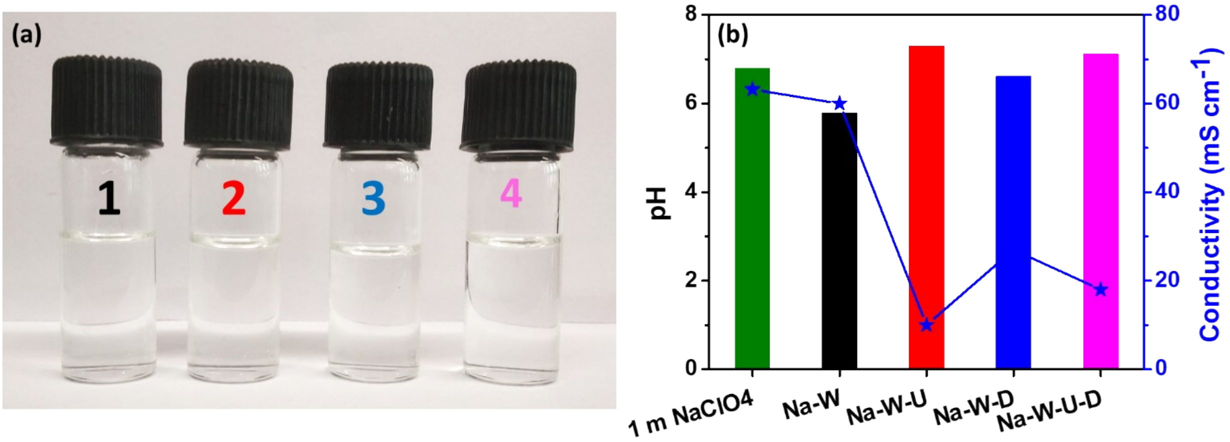

Fig. S5. (a) Photographic images of electrolytes (1) Na-W, (2) Na-W-U, (3) Na-W-D, (4) Na-W-U-D electrolyte, (b) Bar diagram representing conductivity and pH of different electrolytes.

Initially, the pH of 1 m $NaClO_4$ was 6.80, which decreased up to 5.8 for Na-W electrolyte. The pH of electrolytes increases from 5.8 to 7.3, indicating that urea was involved in the solvation structure. However, after adding urea, conductivity falls from 60 to 10 mS cm^{-1}. Further, after adding the DMF, the conductivity of the electrolyte increases from 10 to 18 mS cm^{-1} with small decrease in the pH from 7.3 to 7.1 showing the involvement of both urea and DMF in the solvation structure

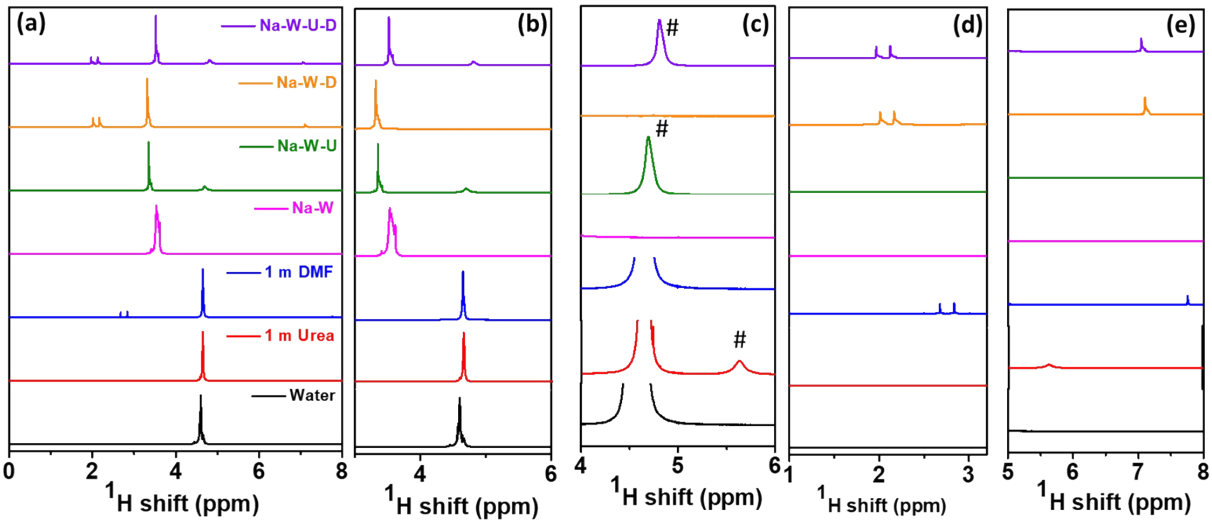

Fig. S6A. (a) ^{1}H NMR spectra, (b)-(e) are the enlarged part of Fig. S6a of various concentrated electrolytes.

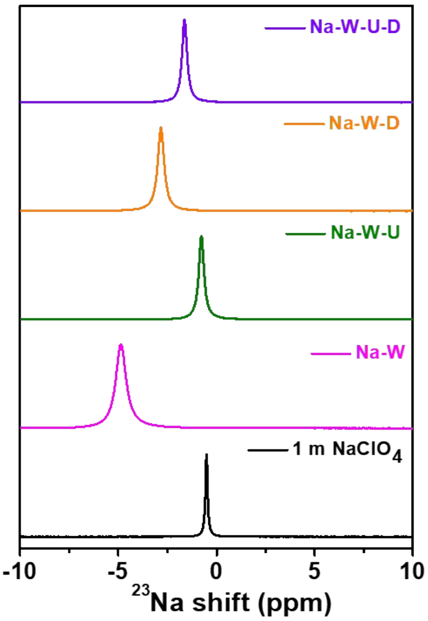

Fig. S6B. ^{23} Na NMR spectra of various concentrated electrolytes.

The ^1H NMR recorded for the pure water shows an intense chemical shift at 4.7 ppm. For 1 m urea and 1 m DMF, proton associated with the water do not shows any significant peak shift. However, in 1m urea, an additional peak can be seen at 5.65 ppm due to N-H proton of urea. Similarly, in DMF we observed a pair of peaks at a chemical shift 2.68 and 2.85 ppm due to the presence of two CH_3 group, and another peak at at 7.78 ppm due COH group. In 17 m $NaClO_4$ (Na-W) electrolyte the peak shifted up to 3.5 ppm. Similar shift we observed in Na-W-U (3.36 ppm), Na-W-D (3.31 ppm) and Na-W-U-D (3.47 ppm) electrolyte. The up field chemical shift (lower chemical shift) is due to the shielding of the water molecules by the additional ions surrounding them. This significant decrease in the water activity is due to reduced free water molecules and increased interaction between salt and these organic molecules with and water.[1-3] Similar up field shield was observed for the proton associated with the urea (5.65 to 4.8 ppm) and DMF (2.68 & 2.85 to 1.96 & 2.11 and 7.78 to 7.02 ppm) showing the significant change in the water solvation structure where some water of the water molecules are replaced by the urea and DMF. Further to understand the Na^+ coordination environment in different electrolyte, ^{23}Na NMR spectroscopy recorded. As indicated in Fig. S8b, similar to the ^1H NMR, the up field chemical shift was noticed the ^{23}Na NMR shows a clear peak at a chemical shift of -0.52 ppm (1 m $NaClO_4$), - 4.85 ppm (17 m $NaClO_4$), -0.8 ppm (Na-W-U), -2.8 ppm (Na-W-D) and -1.67 ppm (Na-W-U-D).

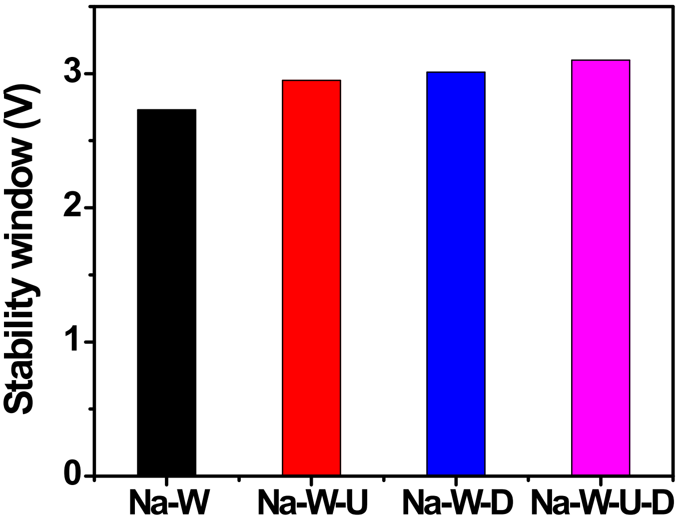

Fig. S6C. (a) Bar diagram representing the electrochemical stability window of different electrolytes.

To eradicate the kinetics effects during the LSV, the ESW of the electrolyte was further determined by following some strict measures. The WE was subjected to the constant cathodic potential from -1.2 to -1.7 V and anodic potential of 1.3 to 1.8 V until the steady current is not reached both in cathodic and anodic directions. From the intercepts of cathodic and anodic current density *vs.* potential plot, the anodic and cathodic limits were determined, leading to an overall stability window of 3.1 V.

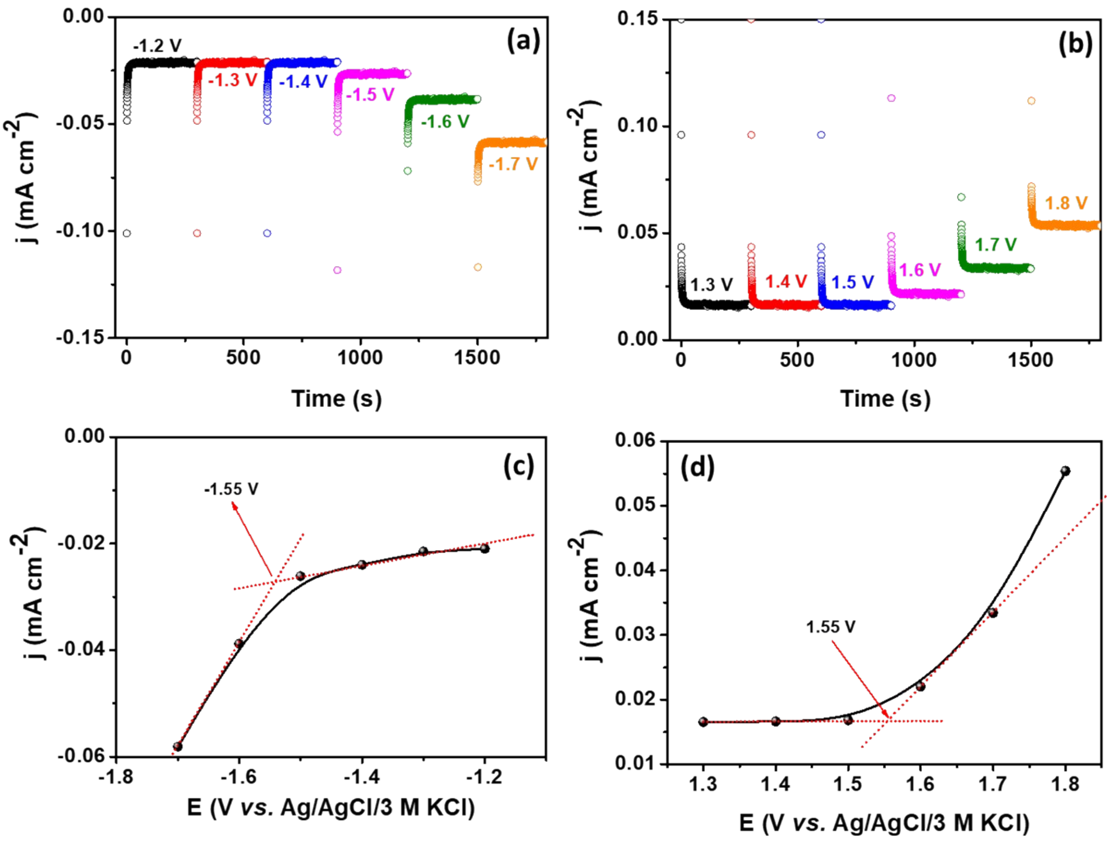

Fig. S7. Sequential chronoamperometric measurements at various (a) anodic and (b) cathodic potentials, (c) and (d) are the plot of anodic and cathodic current density against various potentials.

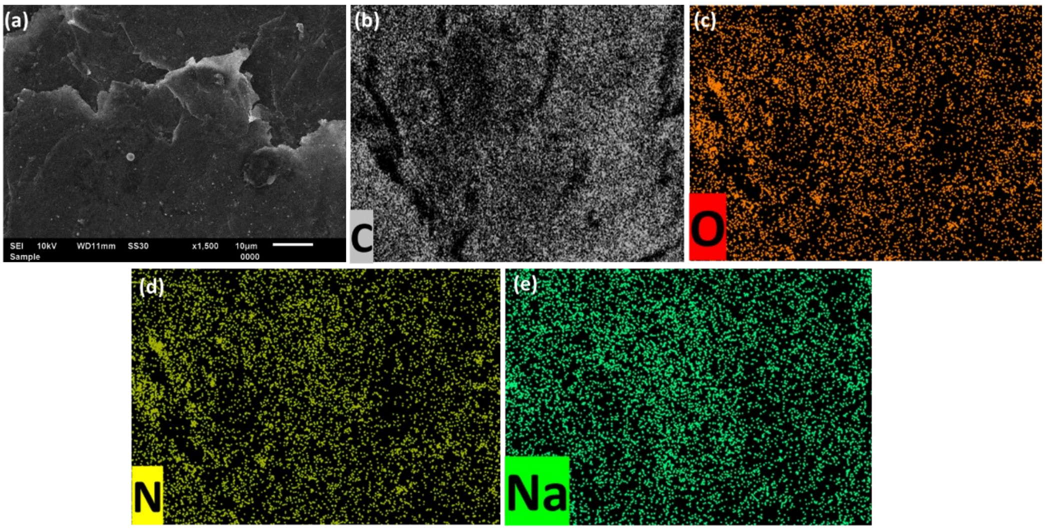

Fig. S8. (a) SEM and corresponding elemental dot mapping images showing the distribution of (b) carbon, (c) oxygen, (d) nitrogen, and (e) sodium for graphite paper working electrode after stability window determination.

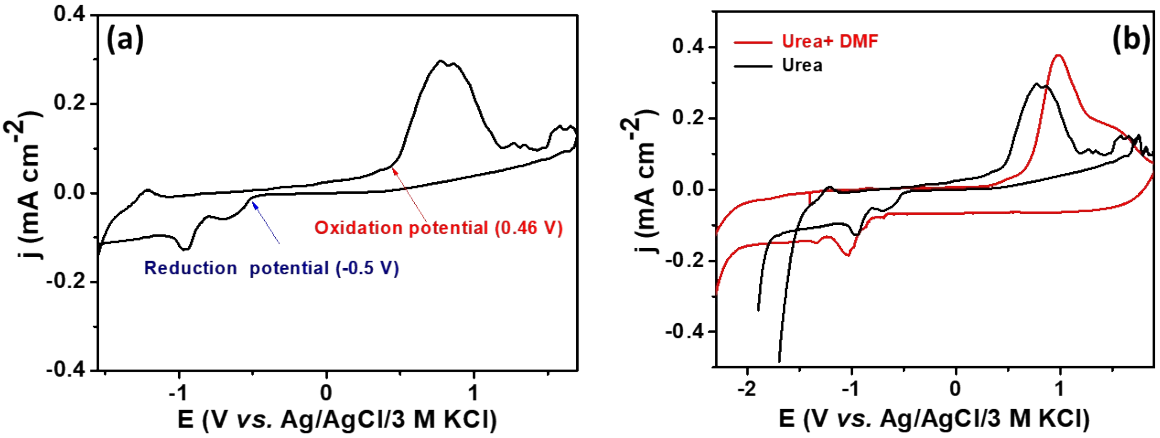

Fig. S9. (a) CV showing oxidation and reduction of 1 m urea and (b) 1 m urea + DMF in 1 m $NaClO_4$/acetonitrile.

Flammability test:

The flammability of the electrolyte was tested by dipping half of the paper sheet in pure DMF and Na-W-U-D electrolyte. After soaking for 3 minutes, the unsoaked part of a paper was set on fire. As shown in Fig. S10, pure DMF (top) easily ignites within a few seconds due to the explosive nature of DMF. In the case of the Na-W-U-D electrolyte, the dipped paper in the electrolyte does not catches fire, showing that the electrolyte is non-flammable.

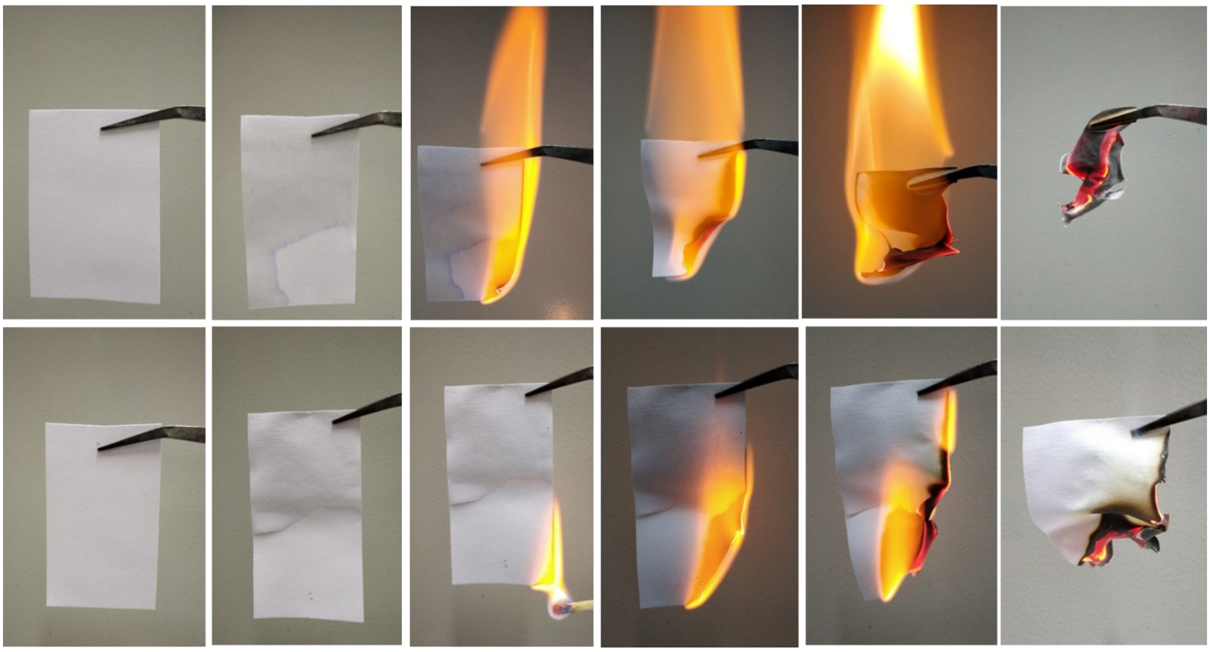

Fig. S10. Visualization studies showing the flammability of the pure DMF (top) and non-flammability of Na-W-U-D electrolyte (bottom).

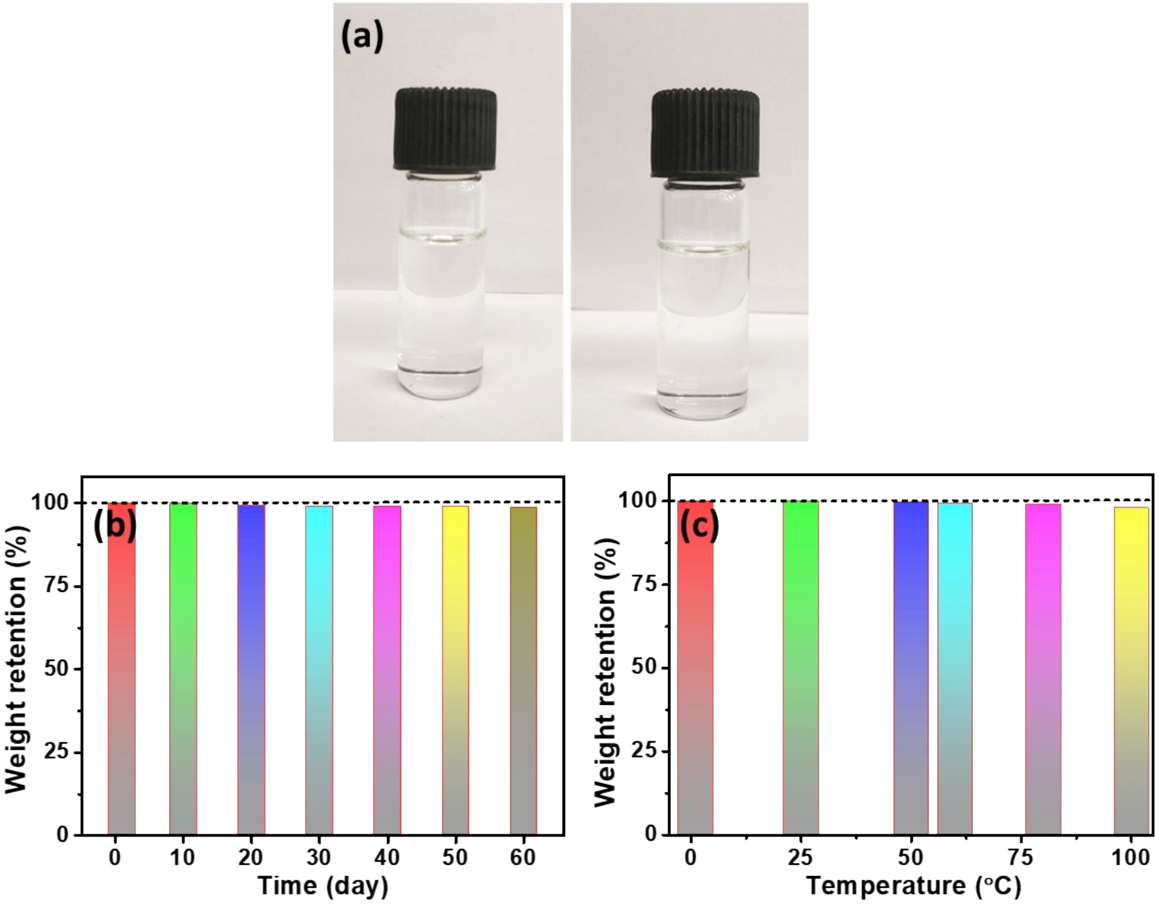

Fig. S11. (a) Photographic image showing electrolyte before and after 60, Bar diagram representing the electrolyte weight retention (b) at room temperature up to 60 days, (c) weight retention at different temperatures for 30 minutes of exposure.

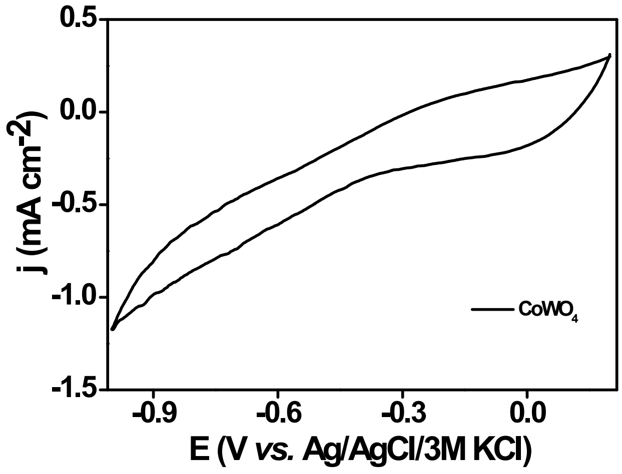

Fig. S12. Cyclic voltammogram of $CoWO_4$ at 1 mV s^{-1} in Na-W-U-D electrolyte, CE: graphite rod, RE: Ag/AgCl/3 M KCl.

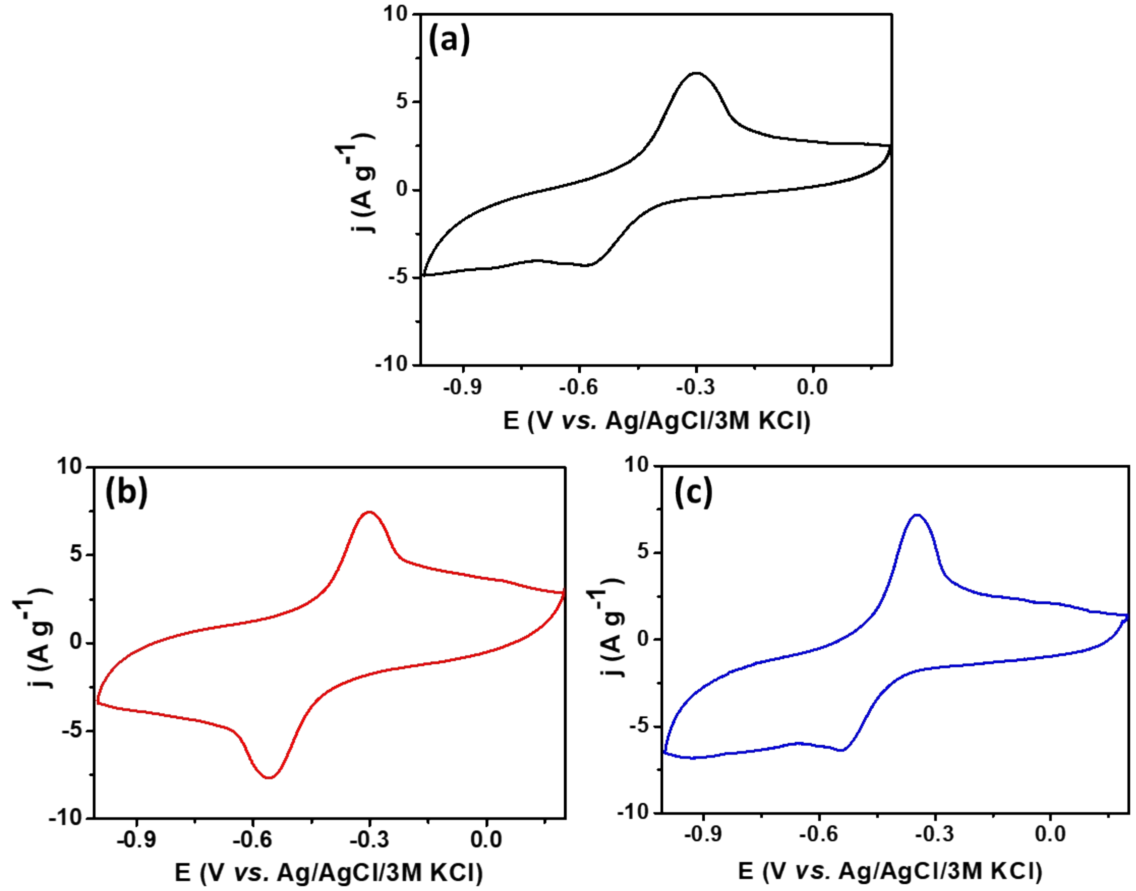

Fig. S13. CVs of S@$CoWO_4$ at 1 mV s^{-1} in (a) Na-W, (b) Na-W-U and (c) Na-W-D electrolyte, CE: graphite rod, RE: Ag/AgCl/3 M KCl.

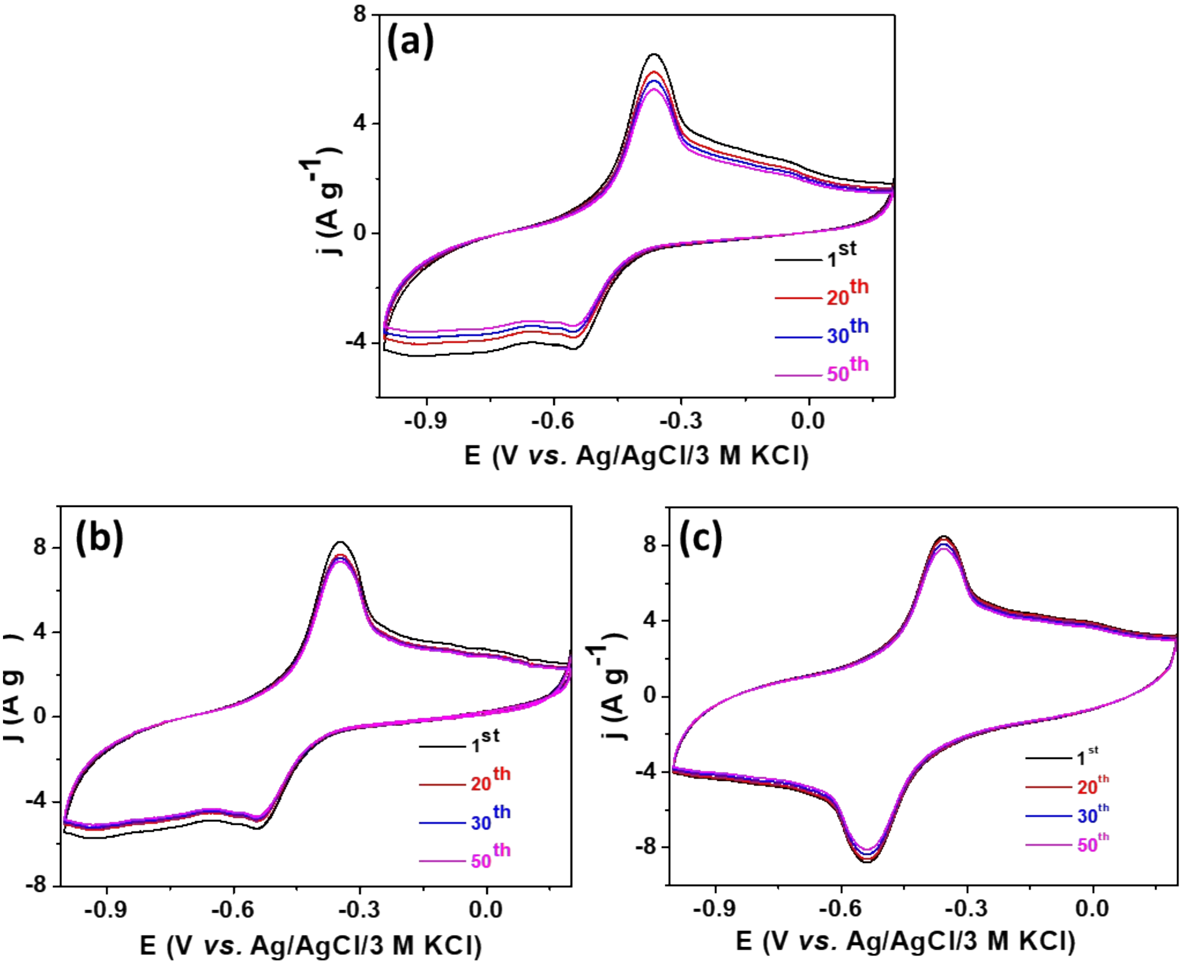

Fig. S14. CVs of S@$CoWO_4$ at 1 mV s^{-1} in (a) Na-W, (b) Na-W-D and (c) Na-W-U electrolyte up to 50 cycles, CE: graphite rod, RE: Ag/AgCl/3 M KCl.

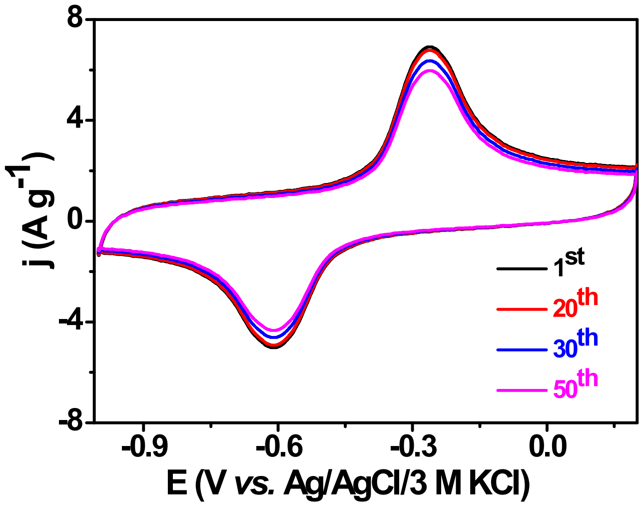

Fig. S15. CVs of S@VC at 1 mV s^{-1} in Na-W-U-D electrolyte up to 50 cycles, CE: graphite rod, RE: Ag/AgCl/3 M KCl.

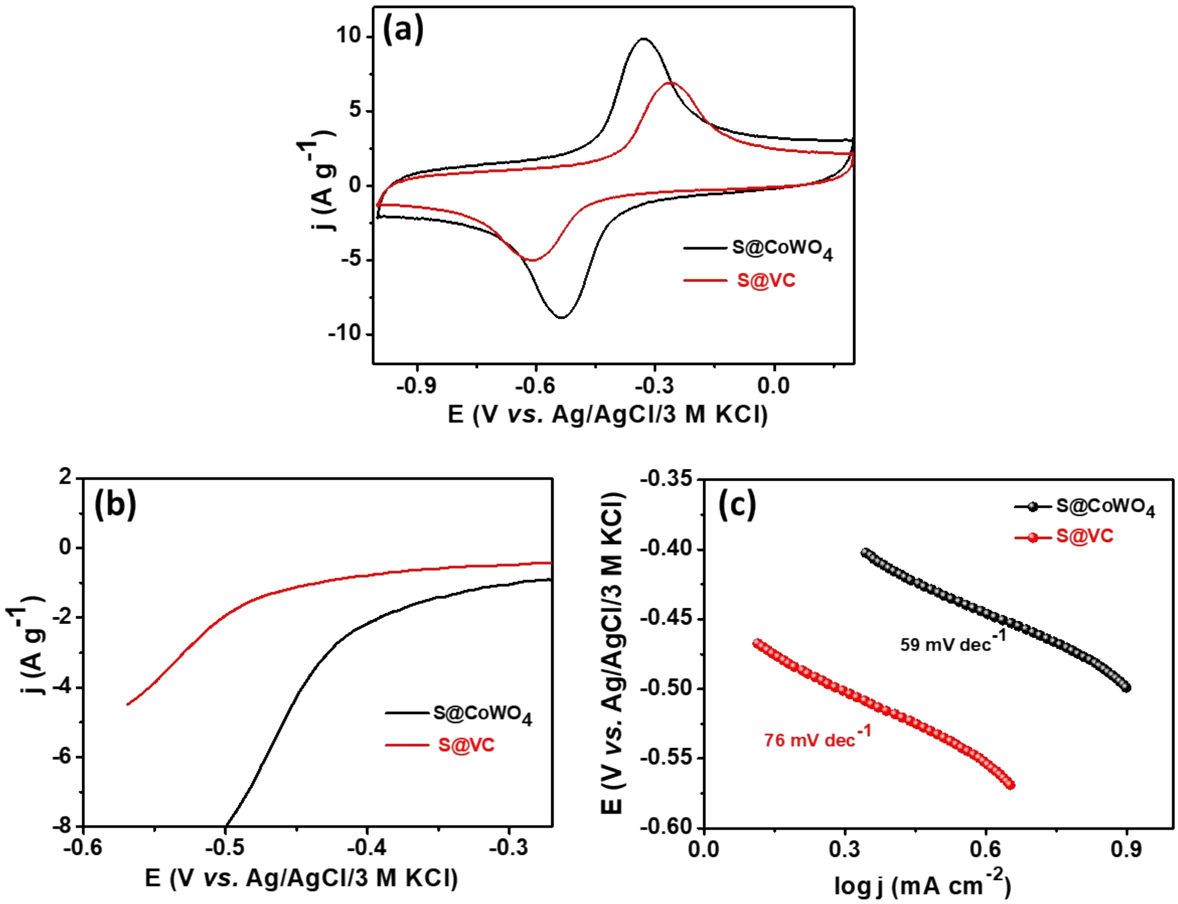

Fig. S16. (a) Comparative CVs of S@$CoWO_4$ and S@VC anode in Na-W-U-D electrolyte at 1 mV s^{-1} (b) linear polarisation curve (zoomed part of CV) representing the onset potential for the reduction of elemental sulfur to sodium polysulfide and (c) corresponding Tafel plot for reduction.

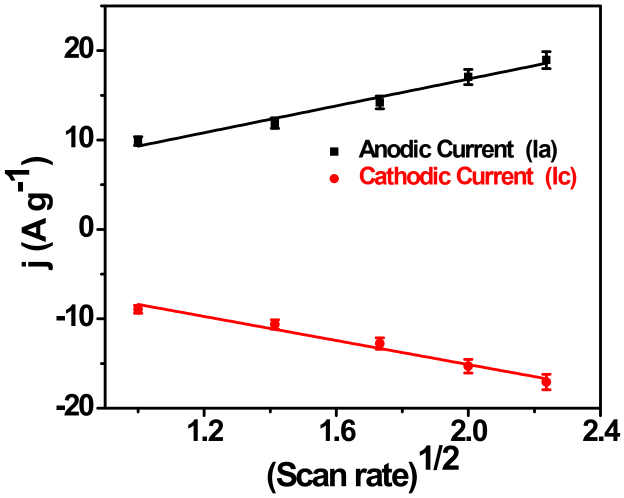

Fig. S17. A plot of anodic and cathodic current density against the square root of scan rates for S@$CoWO_4$.

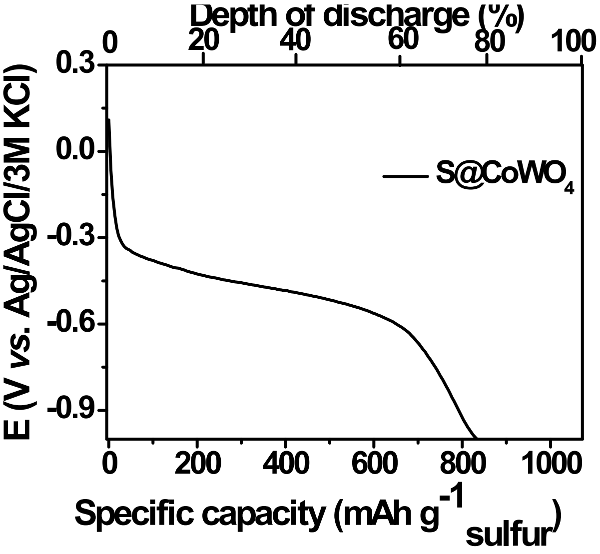

Fig. S18. Discharge curve showing the obtained capacity and depth of discharge @ 0.5 C for the S@CoWO4 anode in Na-W-U-D electrolyte.

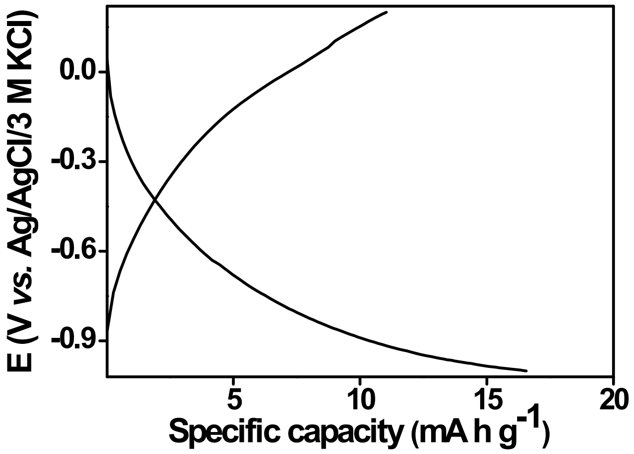

Fig. S19. Voltage profile of $CoWO_4$ at 0.5 C in Na-W-U-D electrolyte, CE: graphite rod, RE: Ag/AgCl/3 M KCl.

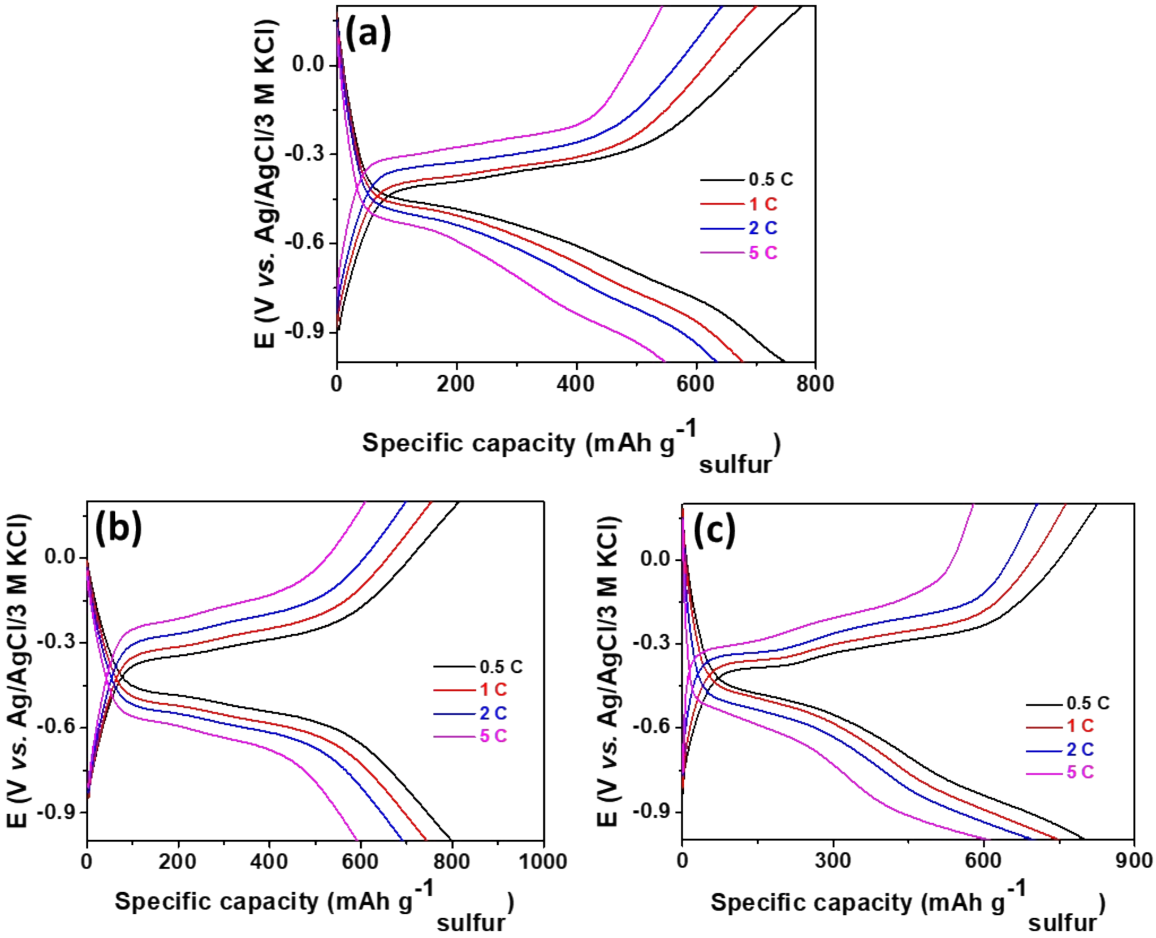

Fig. S20. Voltage profiles of S@$CoWO_4$ at different C-rates in (a) Na-W, (b) Na-W-U and (c) Na-W-D electrolyte, CE: graphite rod, RE: Ag/AgCl/3 M KCl.

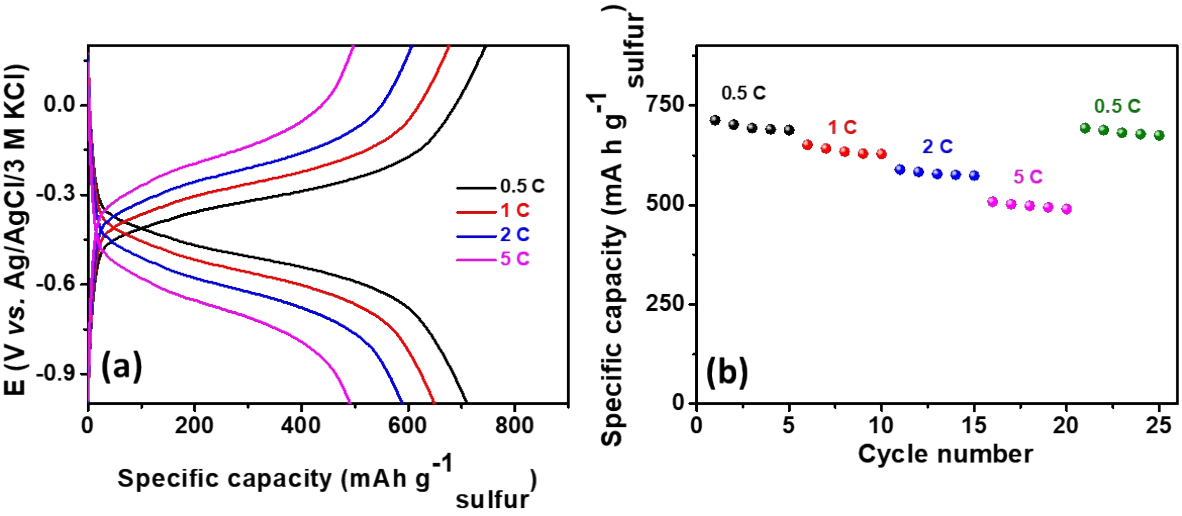

Fig. S21. (a) Voltage profiles and (b) comparison of rate performance of S@VC at different C-rates in Na-W-U-D electrolyte, CE: graphite rod, RE: Ag/AgCl/3 M KCl.

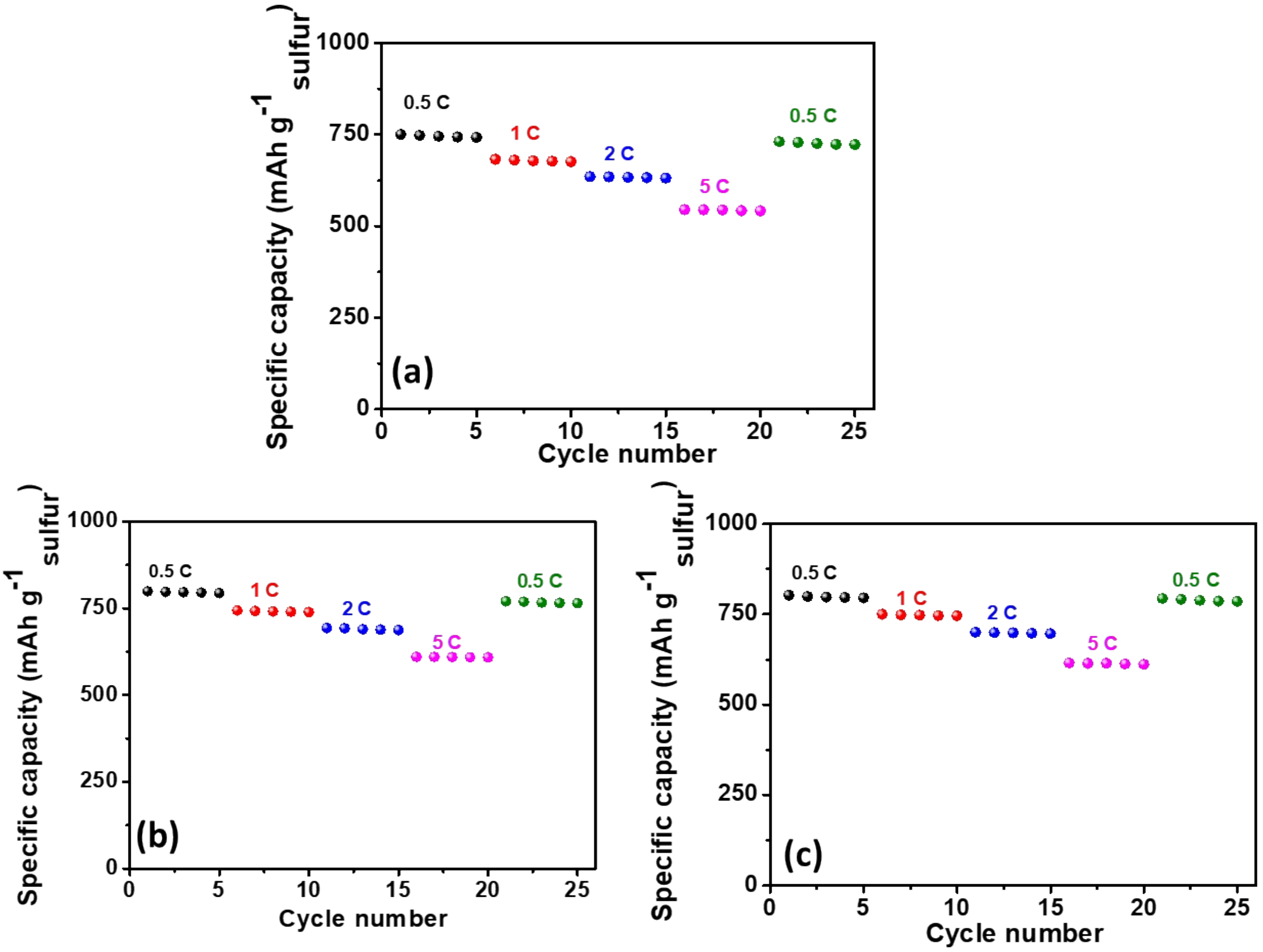

Fig. S22. Rate performance comparison of S@CoWO$_4$ at different C-rates in (a) Na-W, (b) Na-W-U and (c) Na-W-D electrolyte, CE: graphite rod, RE: Ag/AgCl/3 M KCl.

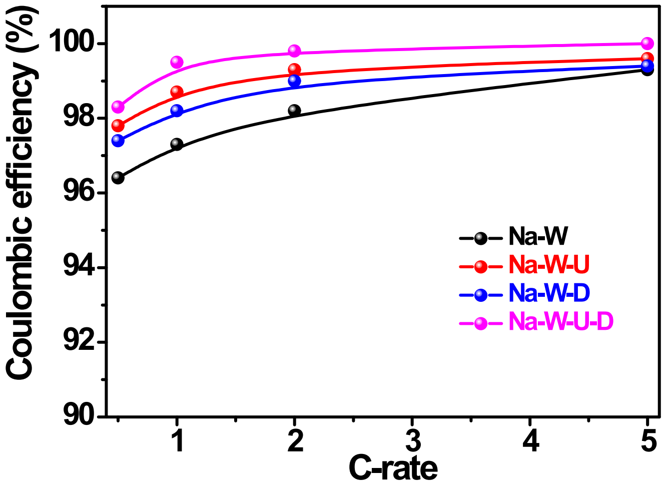

Fig. S23. The CE for S@$CoWO_4$ at different C-rates in different electrolytes, CE: graphite rod, RE: Ag/AgCl/3 M KCl.

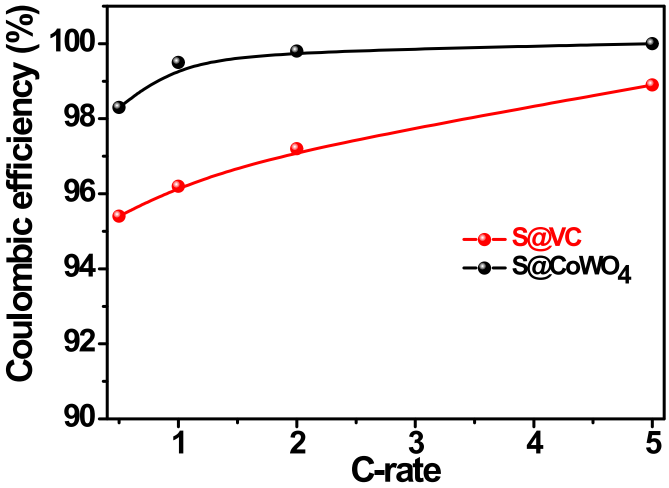

Fig. S24. The CE for S@$CoWO_4$ and S@VC at different C-rates in Na-W-U-D electrolyte, CE: graphite rod, RE: Ag/AgCl/3 M KCl.

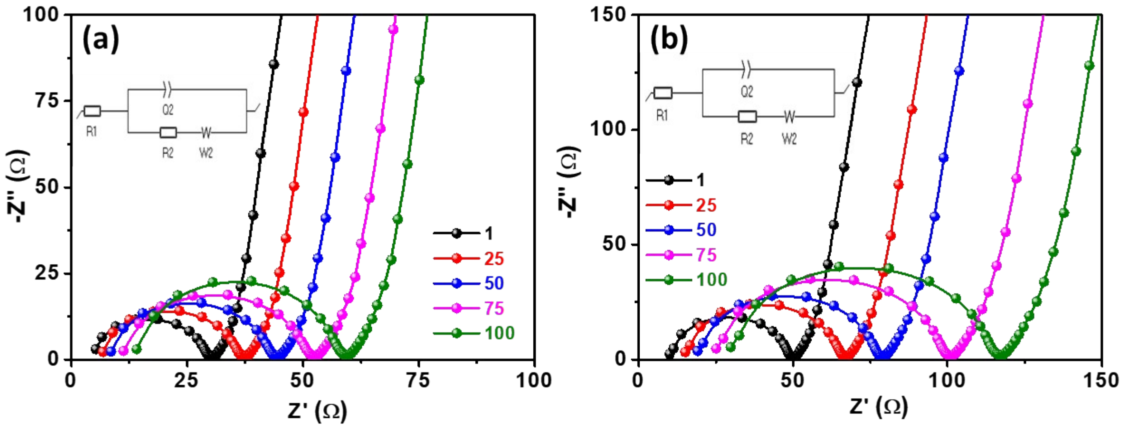

Fig. S25. EIS recorded during the cycling stability for (a) S@$CoWO_4$ and (b) S@VC in Na-W-U-D electrolyte. CE: graphite rod, RE: Ag/AgCl/3 M KCl.

Table S1: Electrochemical Impedance analysis extracted from Fig. 2d and S25.

Cycle No.	**S@$CoWO_4$**			**S@VC**		
	R1(Solution resistance)	**R2(Polarization resistance)**	**R_{ct} = R2-R1**	**R1(Solution resistance)**	**R2(Polarization resistance)**	**R_{ct} = R2-R1**
1	5.25	30.52	25.27	10.25	49.98	39.73
25	6.80	37.39	30.58	15.0325	67.10	52.07
50	8.55	44.71	36.16	19.0375	79.325	60.28

75	11.24	52.50	41.26	25.0475	101.326	76.26
100	14.064	59.52	45.46	29.80	116.8	87.00

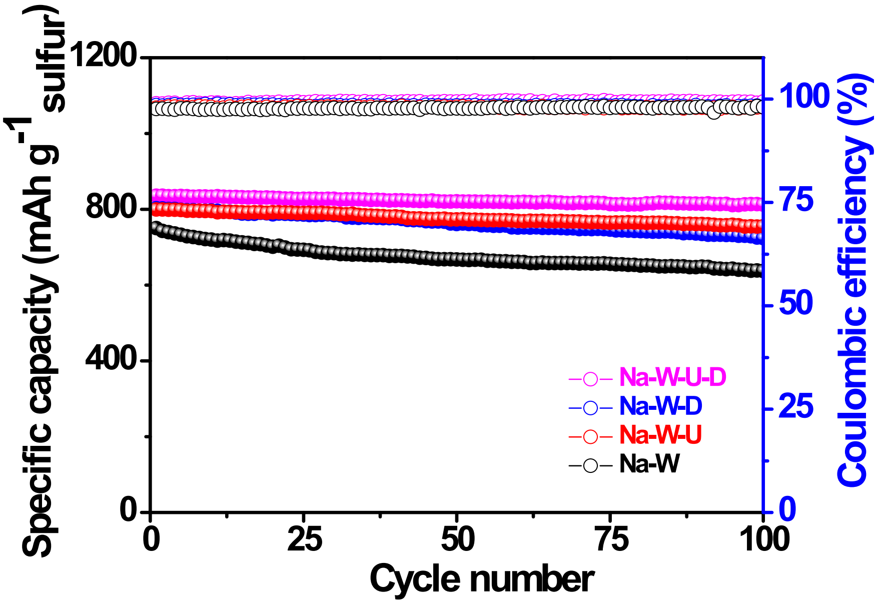

Fig. S26. Cycling stability and corresponding CE of S@CoWO$_4$ at 0.5 C over 100 cycles in different electrolytes. CE: graphite rod, RE: Ag/AgCl/3 M KCl.

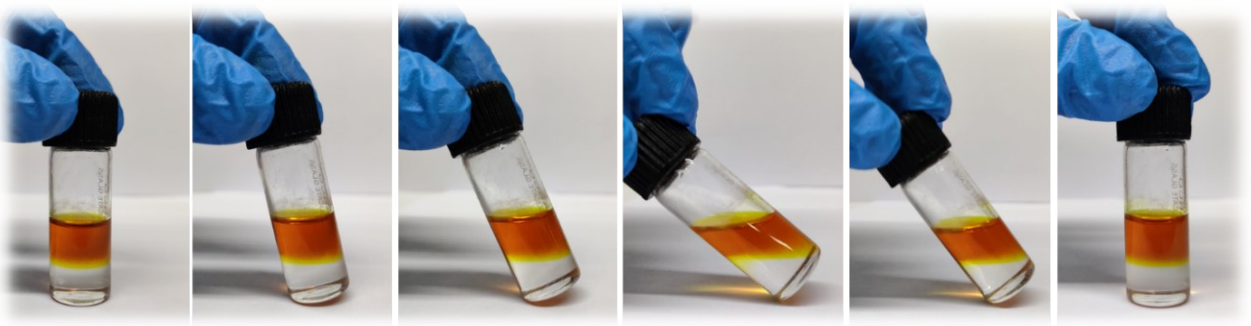

Fig. S27. Visualization studies showing the inhibition of polysulfide dissolution in Na-W-U-D electrolyte.

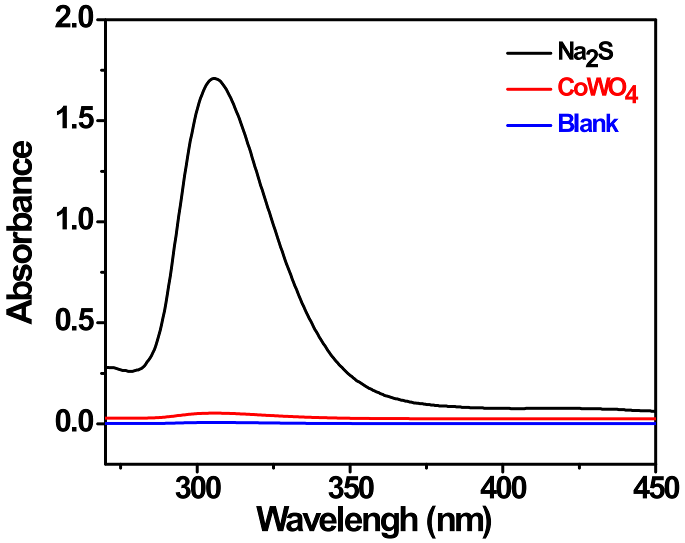

Fig. S28 A. UV-Vis spectra of the electrolyte solution after Na_2S adsorption test.

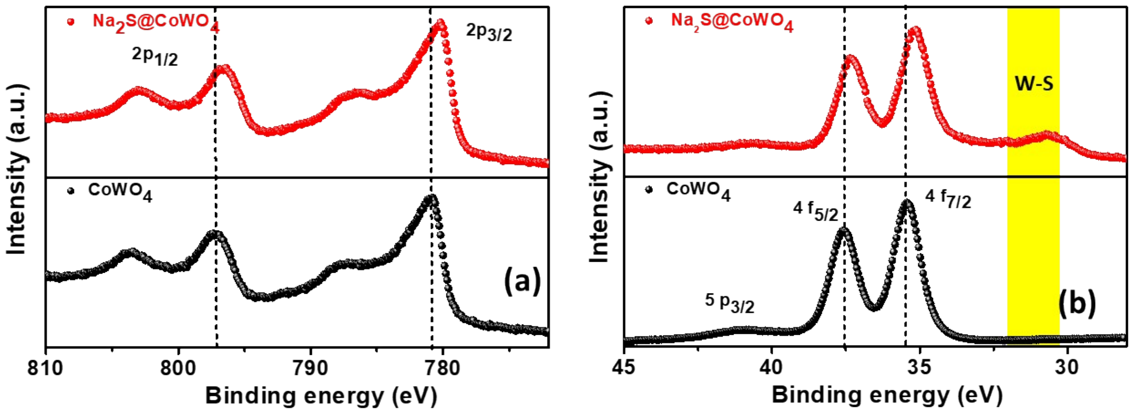

Fig. S28 B. Comparative XPS spectra of (a) Co 2p, and (b) W 4f of $CoWO_4$ before and after the Na_2S adsorption

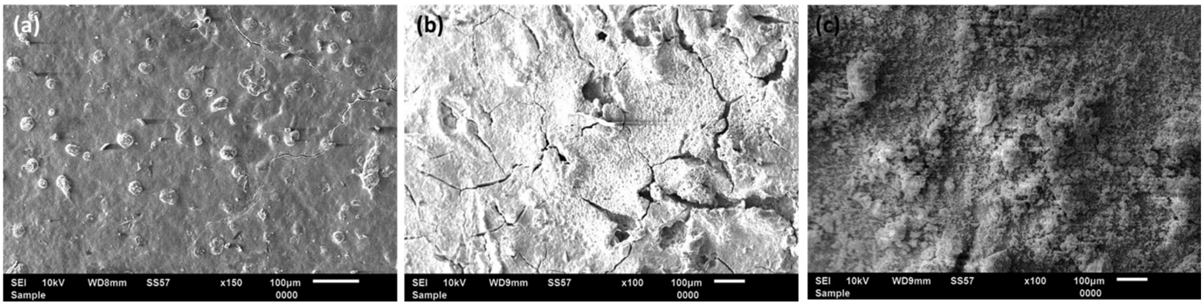

Fig. S29. SEM images of S@$CoWO_4$ after 100 cycles in (a) Na-W-U, (b) Na-W-D, and (c) Na-W electrolyte.

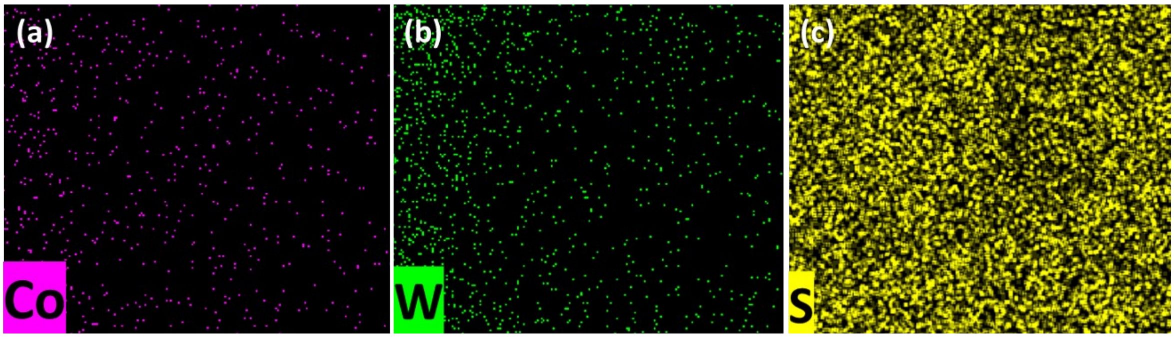

Fig. S30. Elemental dot mapping images showing the distribution of (a) cobalt, (b) tungsten and (c) sulfur after the 100 cycles for S@CoWO$_4$ in Na-W-U-D electrolyte.

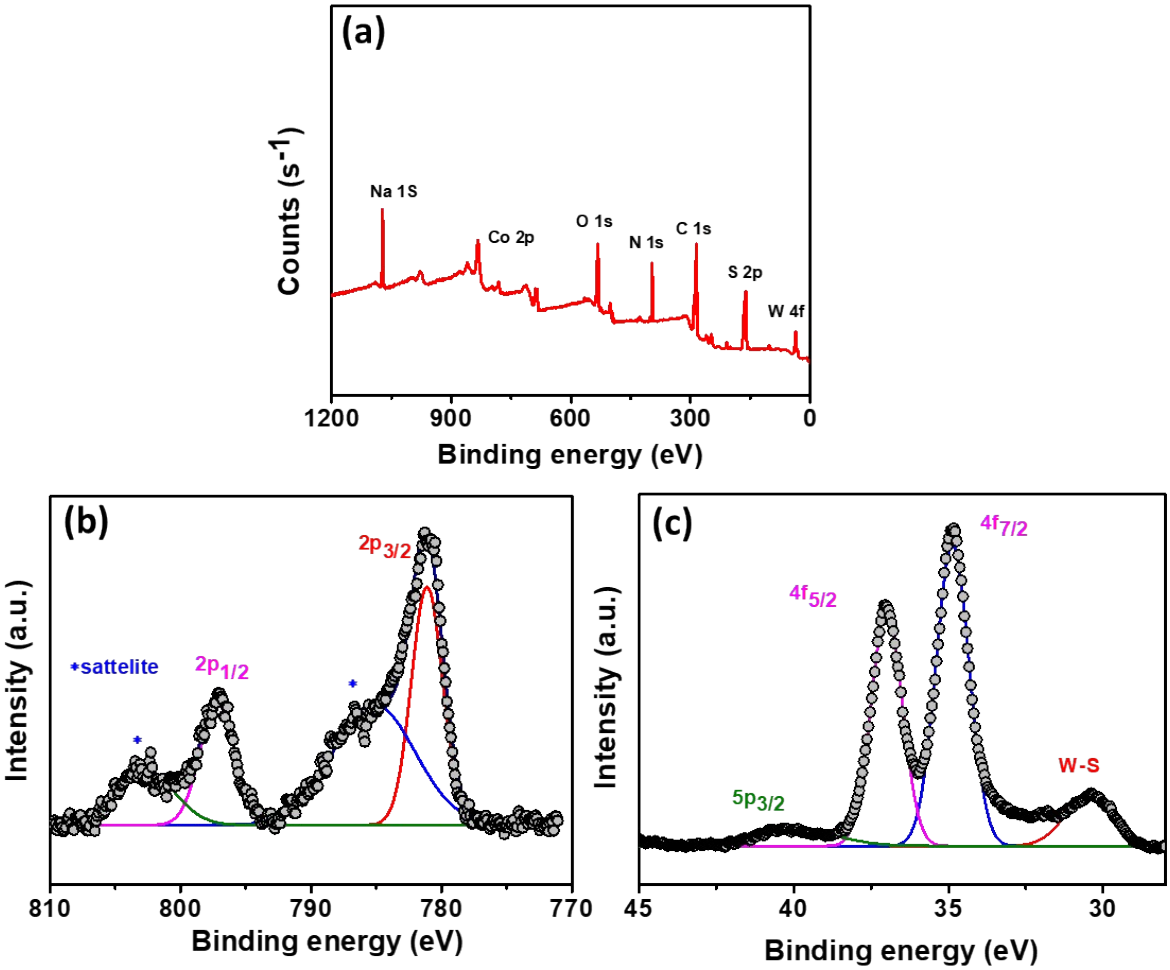

Fig. S31. (a) XPS survey spectra and deconvoluted XPS spectra of (b) Co 2p, and (c) W 4f of S@CoWO$_4$ after stability study.

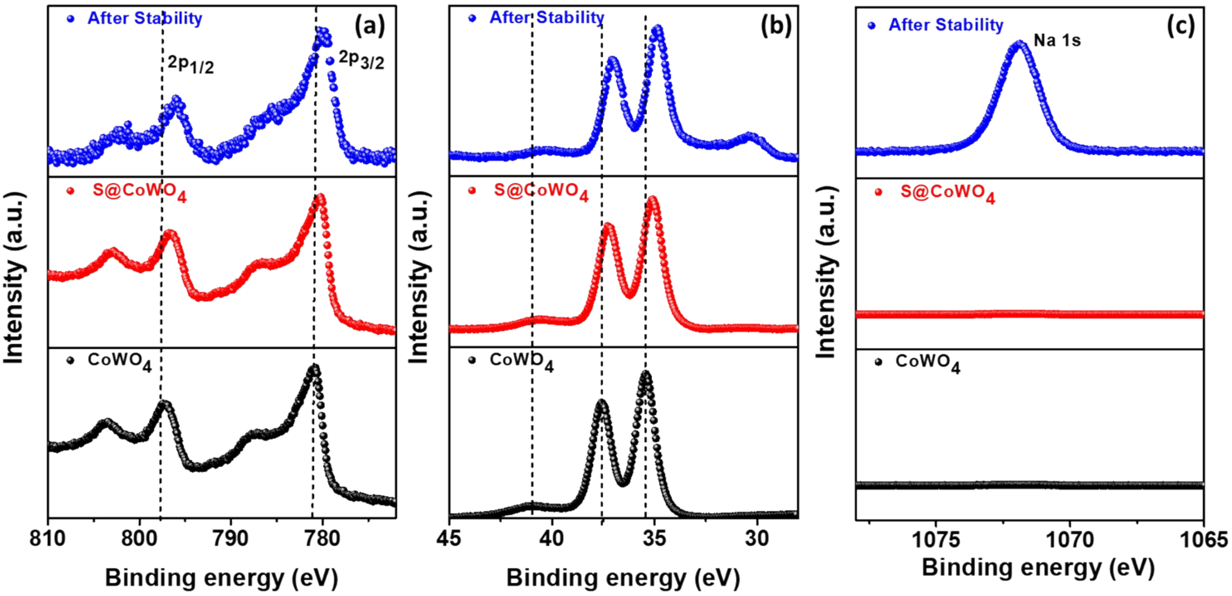

Fig. S32. Comparative XPS spectra of (a) Co 2p, (b) W 4f, and (c) Na 1s of $CoWO_4$, $S@CoWO_4$ before and after stability study.

ORR studies:

To investigate the effect of oxygen on electrocatalytic activity and self-discharge of the anode. The ORR activity of the synthesized catalyst was investigated by hydrodynamic experiments, namely rotating disk electrode (RDE) and rotating ring-disk electrode (RRDE) measurements, in 1 m $NaClO_4$ and Na-W-U-D electrolyte using modular potentiostat/galvanostat (Autolab 302N) with Nova 1.11 software connected with speed controlling unit (AFMSRCE, Pine Research Instrument Inc., USA). Initially, the CV was recorded in O_2 and Ar saturated environment for $CoWO_4$ drop coated glassy carbon (GCE, Ø 3 mm) at 25 mV s^{-1}, over the potential range of 0.6 to -1.0 V (for 1 m $NaClO_4$) and 0.6 to -1.6 V (for Na-W-U-D electrolyte). The hydrodynamic experiments *viz.* RDE and RRDE were performed at various rotation rates between 0 to 1300 rpm at a scan rate of 5 mV s^{-1} using a glassy carbon disk-Pt ring (GC-Pt) ring-disk electrode from Pine Research Instrument Inc., USA) as WE (20 µl) (50 µg) of catalyst slurry drop coated on GCE disk) in a three-electrode assembly. The measurements were performed under both an inert atmosphere (purging with Ar) and in an oxygen (O_2) saturated media by bubbling it through the electrolyte for 30 min before the start of the experiment, and then a constant flow was maintained above the electrolyte throughout measurements.

The no. of electron and amount of H_2O_2 was calculated by using the following equation.

$$n = 4\, I_d / \left[I_d + \left(\frac{I_r}{N} \right) \right]$$

$$\% \; \mathbf{H_2O_2 = 200{*}(\mathit{I_r}/N)/[\mathit{I_d} + \mathit{I_r}/N]}$$

I_d represents the disk current corresponding to the current involved in oxygen reduction and I_r represents the ring current resulting from the oxidation of H_2O_2 formed at the disk, respectively. N is the collection efficiency, whose value for our system is 0.38.

To check the self-discharge of anode material, firstly, S@$CoWO_4$ was fully discharged to -1.0 V and kept on open circuit potential (OCV) in Ar and O_2 saturated environment in 1 m $NaClO_4$ and Na-W-U-D electrolyte. Afterward, the charging experiment was performed, and capacity retention was determined, which is related to the self-discharge.

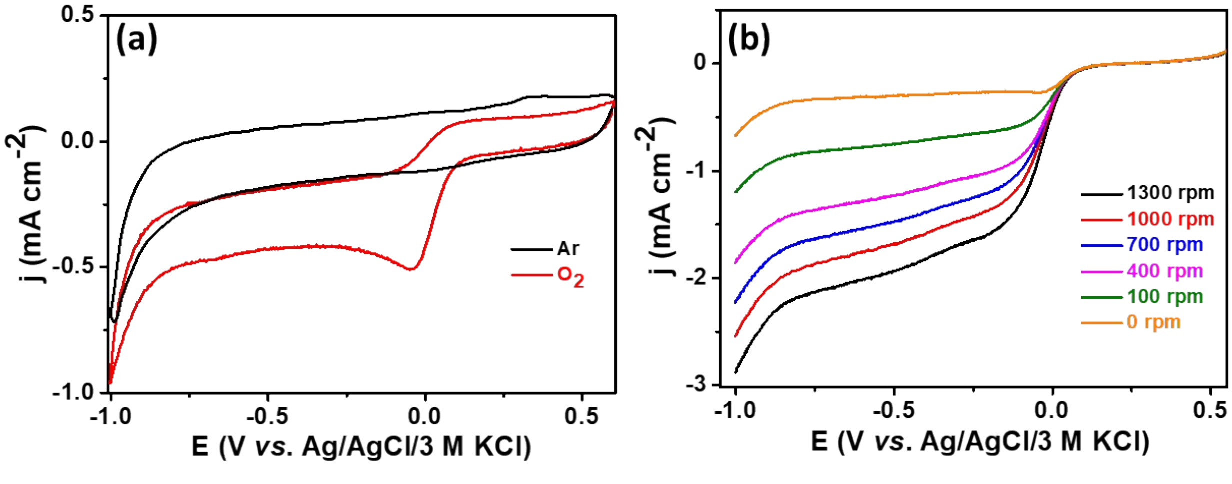

Fig. S33. CVs of $CoWO_4$ in Ar and O_2 saturated 1 m $NaClO_4$, (b) RDE polarization curves for $CoWO_4$ in O_2 saturated 1 m $NaClO_4$ at various rotation rates.

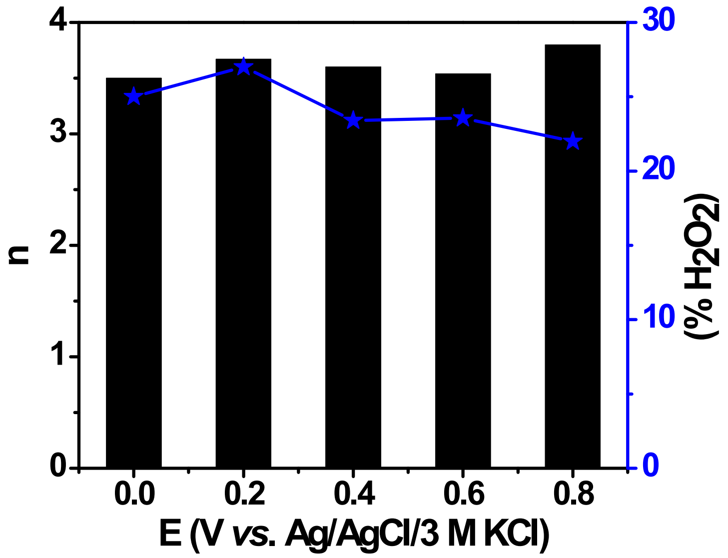

Fig. S34. Bar diagram representing the no. of electron transfer and % H_2O_2 for $CoWO_4$ in 1 m $NaClO_4$ at 1300 rpm.

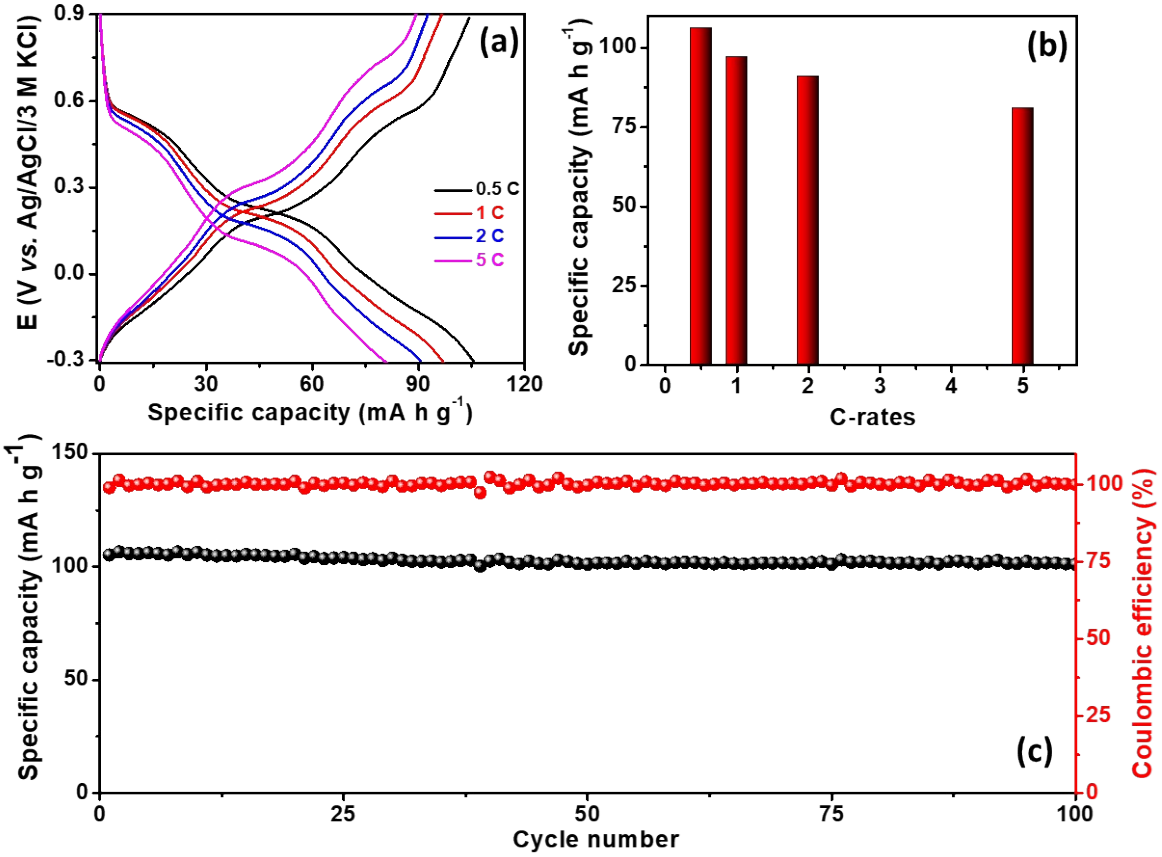

Fig. S35A: (a) Voltage profiles, (b) corresponding capacities at various C rates, (c) cycling stability of $Na_{0.44}MnO_2$ cathode at 0.5 C, in Na-W-U-D electrolyte.

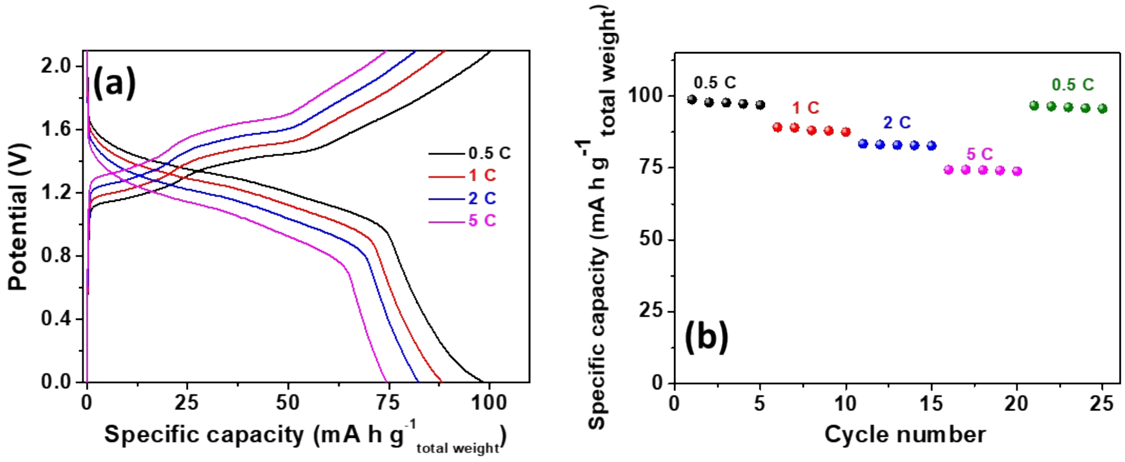

Fig. S35B. (a) Voltage profile and (b) rate performance of full cell battery assembled using S@CoWO$_4$ anode and Na$_{0.44}$MnO$_2$ cathode w.r.t total electrode weight, in Na-W-U-D electrolyte.

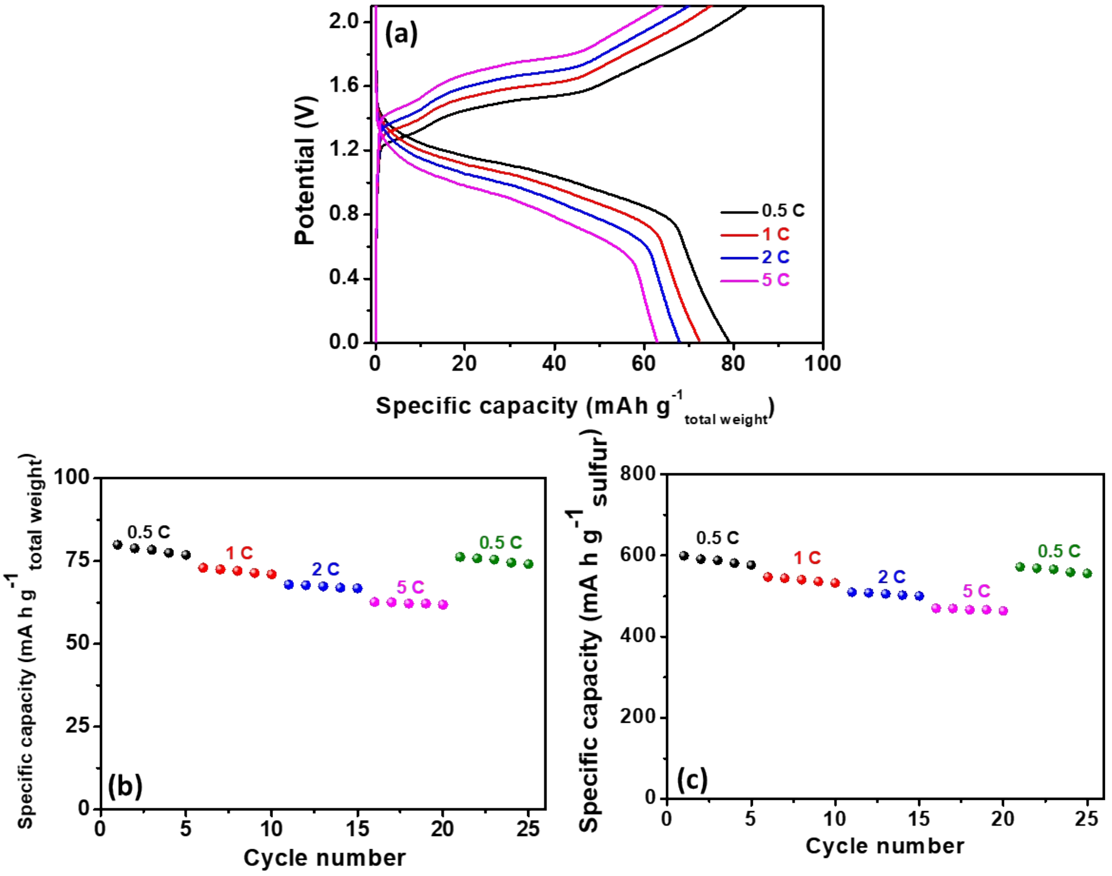

Fig. S36. (a) Voltage profile and corresponding rate performance of full cell battery assembled using S@VC anode and Na$_{0.44}$MnO$_2$ cathode w.r.t (b) total electrode weight, and (c) sulfur weight only in Na-W-U-D electrolyte.

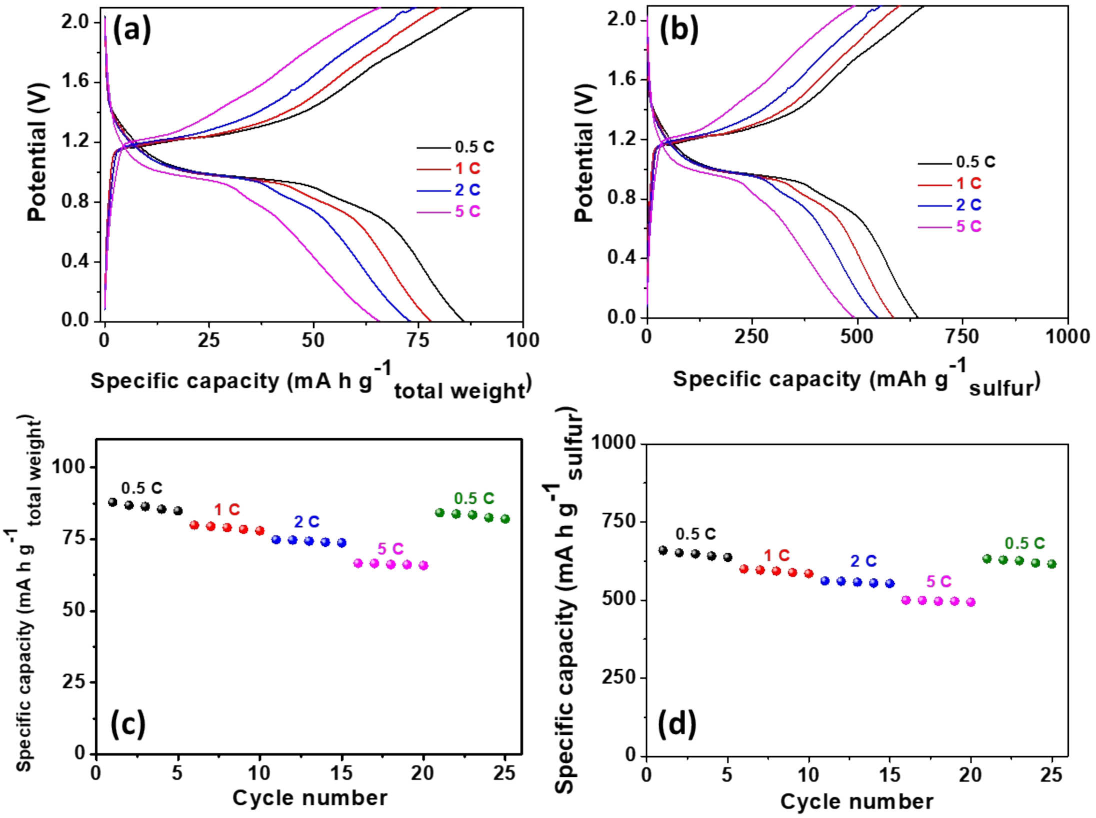

Fig. S37. (a) and (b) Voltage profiles, (c) and (d) corresponding rate performance of full cell battery assembled using S@$CoWO_4$ anode and $Na_{0.44}MnO_2$ cathode w.r.t total electrode weight, and sulfur weight only in Na-W electrolyte.

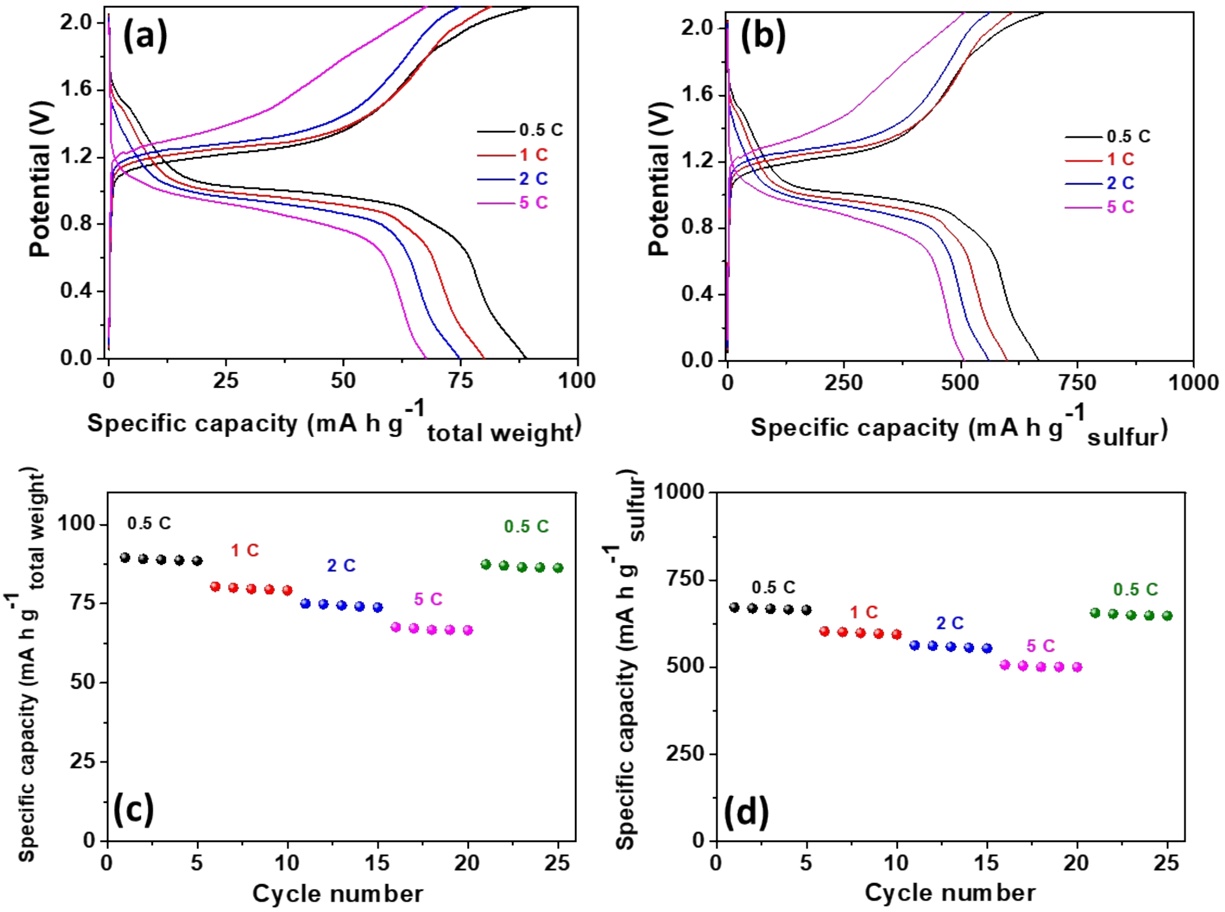

Fig. S38. (a) and (b) Voltage profiles, (c) and (d) corresponding rate performance of full cell battery assembled using S@$CoWO_4$ anode and $Na_{0.44}MnO_2$ cathode w.r.t total electrode weight, and sulfur weight only in Na-W-U electrolyte.

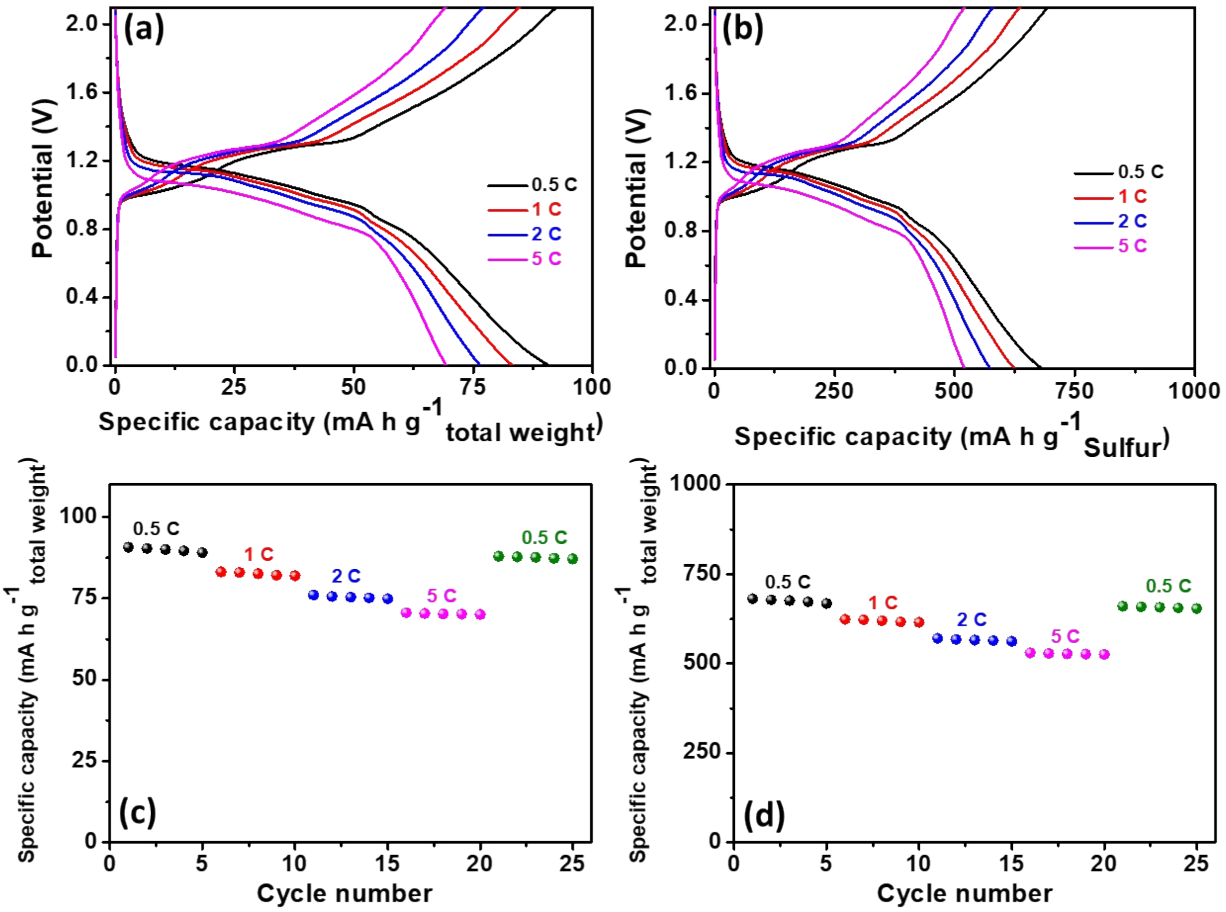

Fig. S39. (a) and (b) Voltage profiles, (c) and (d) corresponding rate performance of full cell battery assembled using S@$CoWO_4$ anode and $Na_{0.44}MnO_2$ cathode w.r.t total electrode weight, and sulfur weight only in Na-W-D electrolyte.

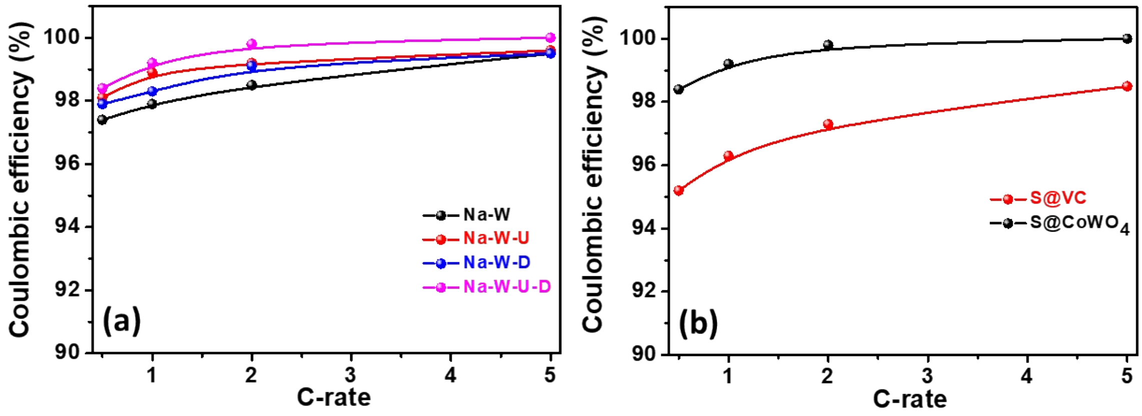

Fig. S40. Comparisons of the CE for a full cell assembled with S@CoWO$_4$ anode and Na$_{0.44}$MnO$_2$ cathode full cell in different electrolytes, (b) S@CoWO$_4$ and S@VC anode + Na$_{0.44}$MnO$_2$ cathode at different C-rates.

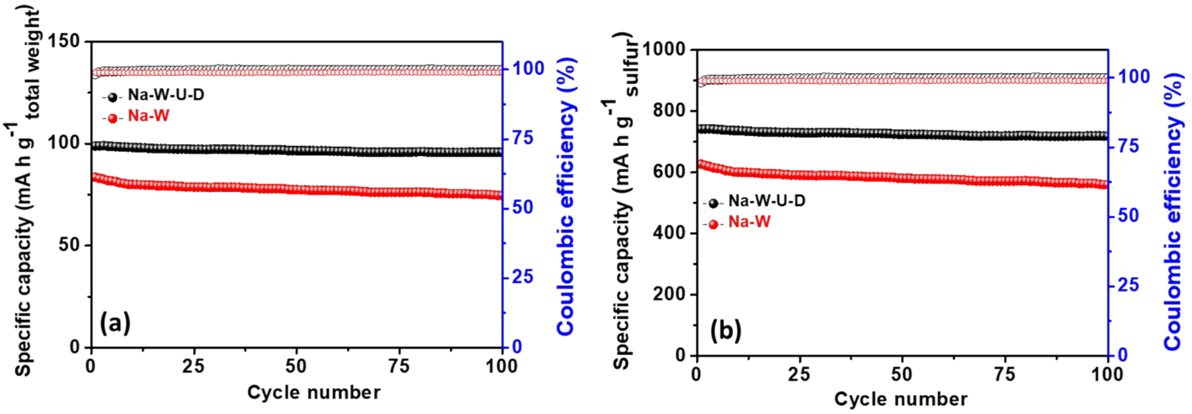

Fig. S41. Cycling stability and corresponding CE of a full cell assembled with S@CoWO$_4$ anode and Na$_{0.44}$MnO$_2$ cathode (a) w.r.t total weight and (b) w.r.t sulfur weight at 0.5 C over 100 cycles in Na-W-U-D and Na-W electrolytes.

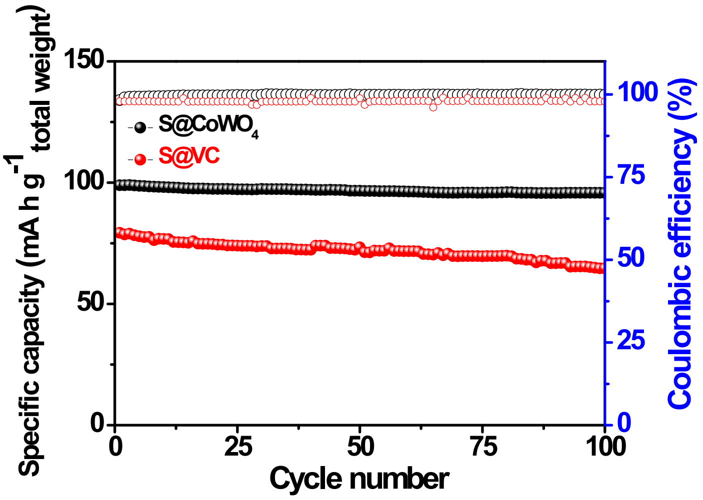

Fig. S42. Cycling stability and corresponding CE of a full cell assembled with S@CoWO$_4$ and S@VC anode and Na$_{0.44}$MnO$_2$ cathode w.r.t total weight at 0.5 C over 100 cycles in Na-W-U-D electrolyte.

Table S1: Comparison of anode material for aqueous sodium-ion battery

S.No.	Anode materials	Capacity (mAh g^{-1})	Ref.
1.	$NaV_3(PO_4)_3$@C hybrid nanofiber	118 (1C)	4
2.	Self-assembled wafer-like porous $NaTi_2(PO_4)_3$	119.4 (1C)	5
3	polyimide–MWCNTs	149	6
4.	Dissolved Polysulfide Na_2S_5	150	7
5.	hydrated $FePO_4$	80 (0.5 C)	8
6.	$Na_3Fe_2(PO_4)_3$	57(2C)	9
7.	$TiNb(PO_4)_3$	119(1C)	10
8.	$Na_2Ti_3/2Mn_{1/2}(PO_4)_3$	88.6 (0.5 C)	11
9.	$Na_3MgTi(PO_4)_3$	54 (0.2 C)	12
11.	**S@$CoWO_4$**	**834 (0.5 C)**	**Our Work**

Table S2: Comparison of energy density for aqueous full cell sodium-ion batteries:

Anode	**Cathode**	**Energy density(Wh kg^{-1})**	**Reference**
$NaTi_2(PO_4)_3$	$Na_2Zn_3[Fe(CN)_6]^{2-}$	55	13
Polyimide	NiHCF@CNTs	45.03	14
$NaTi_2(PO_4)_3$	$Na_{0.44}MnO_2$	27	15
$NaTi_2(PO_4)_3$	$Na_2CuFe(CN)_6$	48	16
NaTi2(PO4)3	ZnHCF	59	17
WO_3	$KVO_x[Fe(CN)_6](VHCF)$	17	18
$NaTiOPO_4$	$Na_{1.88}Mn[Fe(CN)_6]_{0.97}\cdot 1.35H_2O$	71	19
NaTi2(PO4)3	$Na_{0.66}[Mn_{0.66}Ti0.34]O_2$	31	20
S@$CoWO_4$-600	**$Na_{0.44}MnO_2$**	**119**	**This work**

References:

1. L. Jiang, L. Liu, J. Yue, Q. Zhang, A. Zhou, O. Borodin, L. Suo, H. Li, L. Chen and K. Xu, *Adv. Mater.*, 2020, **32**, 1904427.
2. H. Tomiyasu, H. Shikata, K. Takao, N. Asanuma, S. Taruta and Y.-Y. Park, *Sci. Rep.*, 2017, **7**, 45048.
3. J. Xie, Z. Liang and Y.-C. Lu, *Nat. Mater.*, 2020, **19**, 1006-1011.
4. L. Ke, J. Dong, B. Lin, T. Yu, H. Wang, S. Zhang and C. Deng, *Nanoscale*, 2017, **9**, 4183-4190.
5. B. Zhao, Q. Wang, S. Zhang and C. Deng, *J. Mater. Chem. A*, 2015, **3**, 12089-12096.
6. T. Gu, M. Zhou, M. Liu, K. Wang, S. Cheng and K. Jiang, *RSC Adv.*, 2016, **6**, 53319-53323.
7. B. Tekin, S. Sevinc, M. Morcrette and R. Demir-Cakan, *Energy Technol.*, 2017, **5**, 2182-2188.
8. Y. Wang, Z. Feng, D. Laul, W. Zhu, M. Provencher, M. L. Trudeau, A. Guerfi and K. Zaghib, *J.Power Sources*, 2018, **374**, 211-216.
9. S. Qiu, X. Wu, M. Wang, M. Lucero, Y. Wang, J. Wang, Z. Yang, W. Xu, Q. Wang and M. Gu, *Nano Energy*, 2019, **64**, 103941.
10. J. Zhang, L. Chen, L. Niu, P. Jiang, G. Shao and Z. Liu, *ACS Appl. Mater. Interfaces*, 2019, **11**, 39757-39764.
11. P. Lei, K. Liu, X. Wan, D. Luo and X. Xiang, *Chem. Commun.*, 2019, **55**, 509-512.
12. F. Zhang, W. Li, X. Xiang and M. Sun, *Chem. Eur. J.*, 2017, **23**, 12944-12948.
13. M. Shao, B. Wang, M. Liu, C. Wu, F.-S. Ke, X. Ai, H. Yang and J. Qian, *ACS Appl. Mater. Interfaces*, 2019, **2**, 5809-5815.
14. Y. Yuan, D. Bin, X. Dong, Y. Wang, C. Wang and Y. Xia, *ACS Sustain. Chem. Eng.*, 2020, **8**, 3655-3663.
15. Z. Li, D. Young, K. Xiang, W. C. Carter and Y. M. Chiang, *Adv. Energy Mater.*, 2013, **3**, 290-294.
16. X.-y. Wu, M.-y. Sun, Y.-f. Shen, J.-f. Qian, Y.-l. Cao, X.-p. Ai and H.-x. Yang, *ChemSusChem*, 2014, **7**, 407-411.
17. L. Niu, L. Chen, J. Zhang, P. Jiang and Z. Liu, *J. Power Sources*, 2018, **380**, 135-141.
18. P. Jiang, Z. Lei, L. Chen, X. Shao, X. Liang, J. Zhang, Y. Wang, J. Zhang, Z. Liu and J. Feng, *ACS Appl. Mater. Interfaces*, 2019, **11**, 28762-28768.
19. A. Zhou, Z. Xu, H. Gao, L. Xue, J. Li and J. B. Goodenough, *Small*, 2019, **15**, 1902420.
20. L. Suo, O. Borodin, Y. Wang, X. Rong, W. Sun, X. Fan, S. Xu, M. A. Schroeder, A. V. Cresce and F. Wang, *Adv. Energy Mater.*, 2017, **7**, 1701189.